

TR-94-01

2

FINAL REPORT (Grant 91-0278)

Study of the Homogeneity of InP Wafers

AD-A273 658



J.Jiménez and P.Martin and M.Avella

Dto de Física de la Materia Condensada, Facultad de Ciencias,

47011 VALLADOLID

SPAIN

DTIC
ELECTE
DEC 15 1993
S A

This document has been approved
for public release and sale; its
distribution is unlimited.

93-30285



93 12 14 03C

**Best
Available
Copy**

REPORT DOCUMENTATION PAGE

Form Approved
OMB No. 0704-0188

Public reporting burden for this collection of information is estimated to average 1 hour per response, including the time for reviewing instructions, searching existing data sources, gathering and maintaining the data needed, and completing and reviewing the collection of information. Send comments regarding this burden estimate or any other aspect of this collection of information, including suggestions for reducing this burden, to Washington Headquarters Services, Directorate for Information Operations and Reports, 1215 Jefferson Davis Highway, Suite 1204, Arlington, VA 22202-4302, and to the Office of Management and Budget, Paperwork Reduction Project (0704-0188), Washington, DC 20585.

1. AGENCY USE ONLY (Leave blank)	2. REPORT DATE	3. REPORT TYPE AND DATES COVERED	
	July 93	FFinal Report 15-July-91 16 July-93	
4. TITLE AND SUBTITLE		5. FUNDING NUMBERS	
A study of Homogeneity of InP wafers		G-AFOSR-91-0278	
6. AUTHOR(S)			
J. Jiménez, P. Martín, M. Avella			
7. PERFORMING ORGANIZATION NAME(S) AND ADDRESS(ES)		8. PERFORMING ORGANIZATION REPORT NUMBER	
Universidad de Valladolid Facultad de Ciencias Física de la Materia Condensada 47011 Valladolid, Spain			
9. SPONSORING/MONITORING AGENCY NAME(S) AND ADDRESS(ES)		10. SPONSORING/MONITORING AGENCY REPORT NUMBER	
Monitoring/Sponsoring Agency: European office of Aerospace Research and Development, Box 14, FPO NY 09510-0200		TR-94-01	
11. SUPPLEMENTARY NOTES			
12a. DISTRIBUTION/AVAILABILITY STATEMENT		12b. DISTRIBUTION CODE	
Approved for public release; Distribution unlimited			
13. ABSTRACT (Maximum 200 words)			
<p>The homogeneity of InP substrate at both microscope and microscopic scale has been studied by Raman microprobe and photocurrent mapping. Raman microprobe was used for any type of substrate, revealing different structural and electronic properties of different extended defects. This study was correlated with photoetching and a relation between revealed defects and Raman features was established.</p> <p>Sem insulating substrate were analyzed by photocurrent mapping. Three excitation wavelength were used, revealing different sources of non uniformity in these wafers. The technique is shown to be quite sensitive to electrical non homogeneities, concerning the iron distribution across the wafer.</p>			
14. SUBJECT TERMS		15. NUMBER OF PAGES	
InP, homogeneity, Iron, Raman, Photocurrent		76	
16. PRICE CODE			
17. SECURITY CLASSIFICATION OF REPORT UNCLASSIFIED	18. SECURITY CLASSIFICATION OF THIS PAGE UNCLASSIFIED	19. SECURITY CLASSIFICATION OF ABSTRACT UNCLASSIFIED	20. LIMITATION OF ABSTRACT

TR-94-01

This report has been reviewed and is releasable to the National Technical Information Service (NTIS). At NTIS it will be releasable to the general public, including foreign nations.

This technical report has been reviewed and is approved for publication.



MARC R. HALLADA, Lt Col, USAF
Ballistic Missile Defense Research Coord



DONALD R. ERBSCHLOE, Lt Col, USAF
Chief, International Programs

Accesion No:	
NTIS	CRASH
DTIC	1AB
Unnumbered	U
Justification	
By	
Distribution /	
Availability Codes	
Dist	Avail. of or Special
A-1	

DTIC QUALITY INSPECTED 3

OUTLINE

1.-Introduction

2.-Experimental and Samples

3.-Chemical etching, Optical Microscopy and PSM (Phase Stepping Microscopy).

4.-Raman spectroscopy.

5.-Spatially Resolved Photocurrent (SRP)

6.-Conclusion

I.- INTRODUCTION

Optoelectronic and electronic devices based on InP are needed for optical communication systems. These systems are built up by integrating optoelectronic and electronic devices. The achievement of this integration requires well defined InP substrate specifications. The integration of these devices includes both growth of epitaxial layers and direct incorporation of the devices onto the substrate. The uniformity of the device parameters is strongly dependent on the properties of the substrate wafers and more specifically on their homogeneity at both long and short range, as far as the integration levels are increased. This is critical in the InP technology because the actual state of the art of bulk crystal growth produces rather defect rich crystals. Actually, a need for the understanding of the wafer homogeneity at both short and long range scales is priority for the crystal growers and the device makers in order to improve the substrate quality and hence the device homogeneity.

Both as grown defects and defects induced during processing are critical to the development of OEIC and integrated high speed devices, affecting their performance, reliability and fabrication yield (1). Among the requirements that the wafers must fulfill, the crystal homogeneity is fundamental to the device fabrication yield and reliability. The uniformity of the device performance, both electrical and optical, across the wafer at the macroscopic and microscopic scale is necessary. We need then:

High resistivity wafers ($10^7 \Omega\text{-cm}$)

Large diameter (100) wafers

Uniform electronic properties

Uniform structural properties

InP wafers are characterized by strong non uniformities associated with the presence of grown-in extended defects, such as dislocations, twins, precipitates and inhomogeneous dopant distribution, which varies from seed to tail of the ingot and from the growth axis to the periphery, forming characteristic doping growth striations (1,2); a summary of these defects is presented in fig.1. In addition to this, defects induced during the wafer preparation need to be studied, because they can have serious negative consequence on the epitaxial layers grown on these substrates. Among these defects subsurface damage

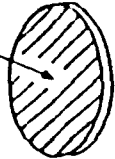
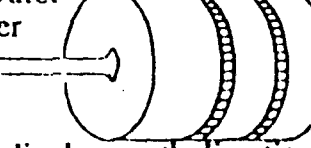
	
microscale (dimensions < 100μm)	
<ul style="list-style-type: none"> * doping striations * precipitates * dislocation clusters * strainfields around dislocations and precipitates 	<ul style="list-style-type: none"> * doping striations * precipitates — —
macroscale (dimensions > 1mm)	
<ul style="list-style-type: none"> * dopant concentration (p, a_0) * dislocation density (EPD) * strain fields 	<ul style="list-style-type: none"> * dopant concentration — —

Figure 1: The various natures of non-uniformity in InP bulk crystal caused during growth.

and oxidation occupy a prominent place (3,4).

The study of these non homogeneities is of high interest not only for the devices makers~ that need routine characterization procedures, but also for the crystal growers that need to understand the nature and the origin of the defects in order to improve the crystal growth parameters.

An important point to consider when dealing with InP is the surface preparation, different problems are critical to the surface quality. The first one is the oxidation of the surface; in fact InP surfaces are quickly oxidized when exposed to ambient and usually the InP wafers are not ready to use (5).

A second point is the damage of the surface produced by polishing. InP is a material difficult to handle due to its brittleness. Usually after chemical etching strong subsurface damage is observed, which is a result of the polishing procedure, this damage cannot be observed in a first inspection after polishing.

The present study was carried out using **Raman spectroscopy and photocurrent** as the main experimental techniques. Another technique is used as an auxiliary tool; this is the **chemical photoetching**. The selective revelation of defects is observed by **Optical Interference Microscopy (Nomarski)** and by **PSM (Phase Stepping Microscopy)**

The study by Raman spectroscopy is devoted to the conditions of the wafer surface, due to the limitations of the Raman probe depth for visible light excitation. Different semiinsulating, Fe doped, undoped, semiconducting n-type, either Sn or S doped, and p-type, either Cd or Zn doped, samples were studied. Long range homogeneity, across the wafer diameter, and microscopic crystallographic defects are studied, in particular twin lamellae, that are frequently present in InP crystals, growth striations, faceting and grown- in dislocations.

The study of spatially resolved photocurrent is focused on iron doped semiinsulating material (6). These measurements are used to reveal different electric non uniformities; as it will be stated later they provide a bulk inspection of the commercial wafers looking

for the iron distribution at both the macroscopic and the microscopic range.

EXPERIMENTAL TECHNIQUES AND SAMPLES

The main experimental techniques used for the characterization were MicroRaman and Spatially Resolved Photocurrent (SRP) also selective chemical etching procedures were used for the revelation of extended defects. In this paragraph we will describe the main characteristics of the experimental setups. The capabilities of the techniques will be described in the corresponding paragraphs, where the results will be presented.

MicroRaman

The microRaman system was a Dilor X~Y equipped with a metallographic microscope fig.2. The excitation sources were the different lines of an Ar laser. In a Raman microprobe working under point illumination both the excitation and scattered light collection are made through the microscope objective; therefore the Raman spectrum is recorded in nearly backscattering configuration. The spatial resolution is diffraction limited and depends on the characteristics of the objective and the laser wavelength; the diameter, D, of the incident laser beam on the sample surface corresponds to the corresponding diffraction spot, which for a microscope objective is given by the following relationship (7) :

$$D = 1.22 \lambda / NA$$

where λ is the laser wavelength and NA is the numerical aperture of the objective.

Most of the measurements were carried out with the 488.0 nm line of an Ar⁺ through a X 100 objective that has a numerical aperture of 0.95. Therefore the diameter of the spot on the focal plane (sample surface) that basically limits the spatial resolution is 0.63 μ m; which due to the small Raman probe depth, \approx 100 nm, is the lateral resolution of the Raman microprobe for the above described experimental conditions.

The Raman probe depth depends on the excitation wavelength and is given by $1 / 2\alpha$,

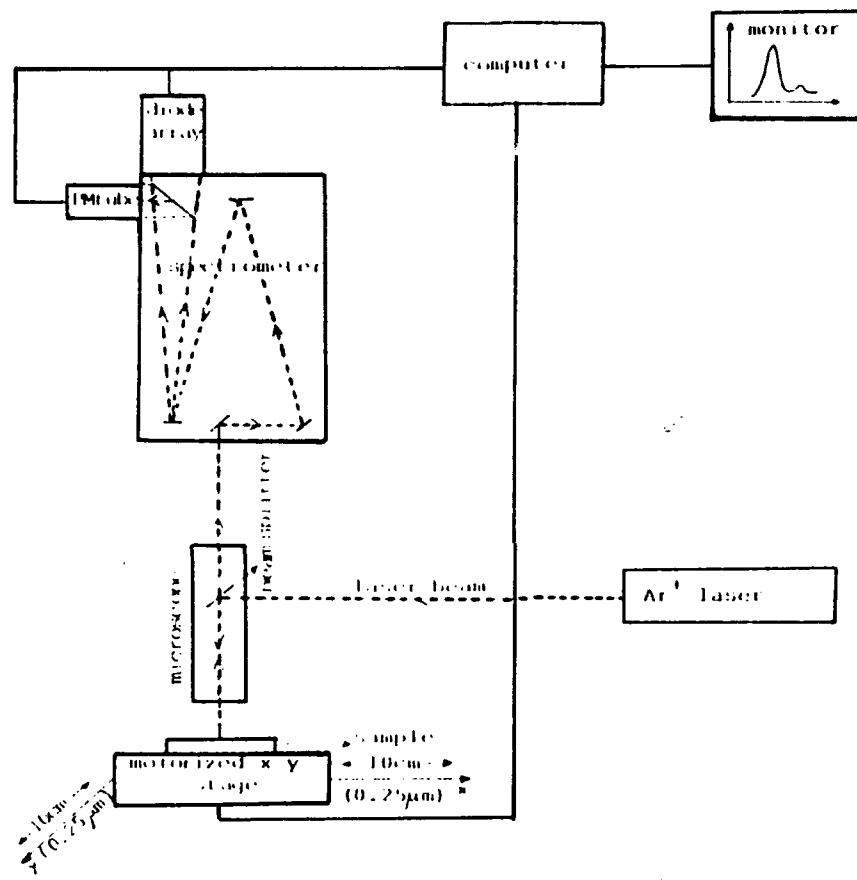


Figure 2: MicroRaman set-up.

where α is the absorption coefficient of InP for the excitation wavelength. For 488.0 nm the Raman probe depth is approximately 100nm (8), which is smaller than the expected damaged depth in handled InP.

Photocurrent

Photocurrent measurements were carried out in two different ways. Conventional photocurrent measurement were devoted to the study of the photocurrent spectrum in order to interpret the main electronic transition taking place in Fe doped InP. These conventional measurements were carried out at different temperatures from 77 K to 300 K. The experimental setup basically consists of a light source halogen lamp a monochromator, a cryostat and an electrometer.

The study of the wafer homogeneity by means of photocurrent measurements is made through an experimental set up developed in our laboratory~ the so-called **photoconductor microscope** (9)

The Spatially Resolved Photocurrent (SRP) system consists of an illumination source a metallographic microscope a cryostat adapted to the X-Y stage of the microscope, a motorized X-Y stage and the acquisition data system. A block diagram of the experimental set up is shown in fig.3.

The spatial resolution depends on the light source used, a halogen lamp or a laser and the characteristics of the microscope objective used for the measurement. With non coherent light excitation (halogen lamp) the spatial resolution is given by the microscope field. With the laser source the resolution is diffraction limited and the spot size is governed by the same relationship that limited the spot size of the Raman microprobe. It should be noted that in this case the sample is transparent to the radiation used which will give a small dispersion of the incident beam for thick samples. Other factors affecting the spatial resolution can be the scanning speed and intrinsic aspects as the minority carrier diffusion length.

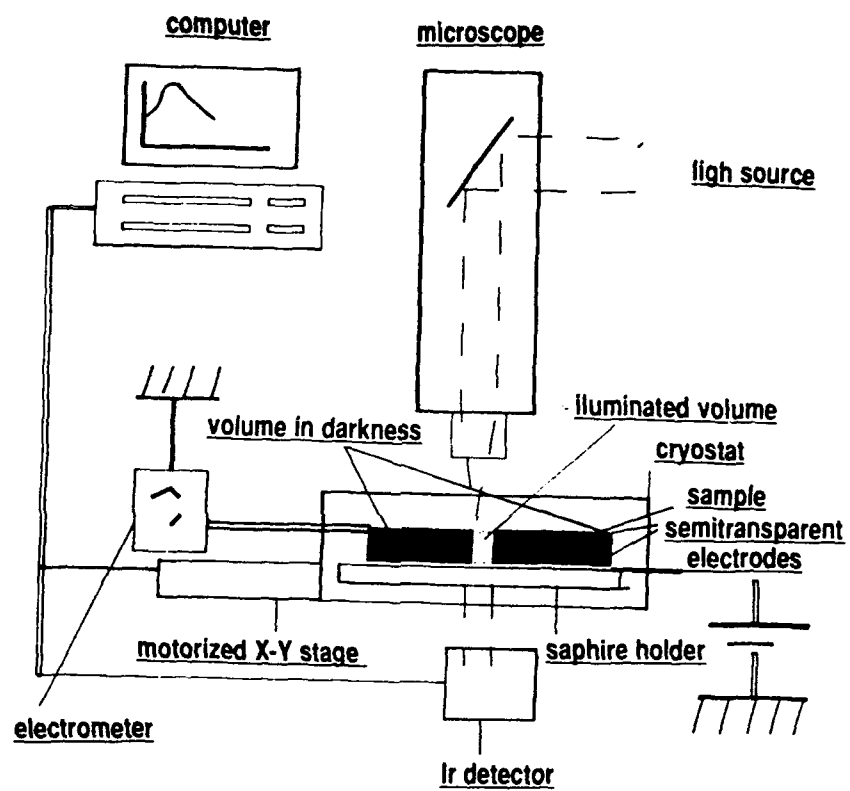


Figure 3: Photoconductor microscope.

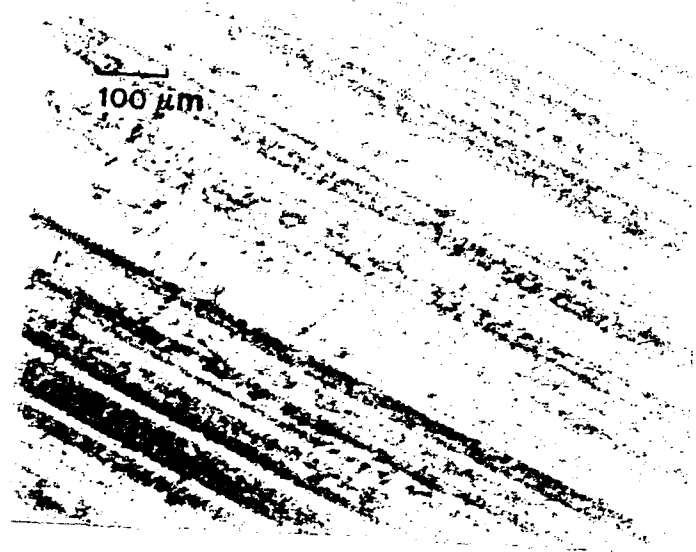


Figure 4: Growth striations (InP:Fe) (Nomarski micrograph).

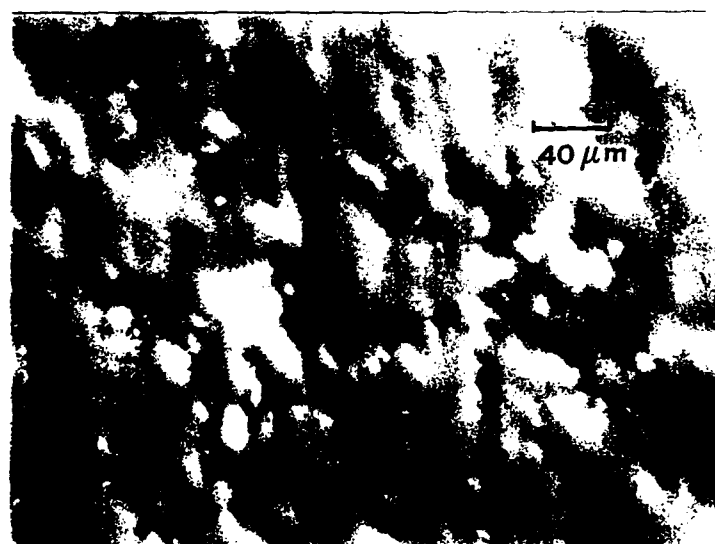
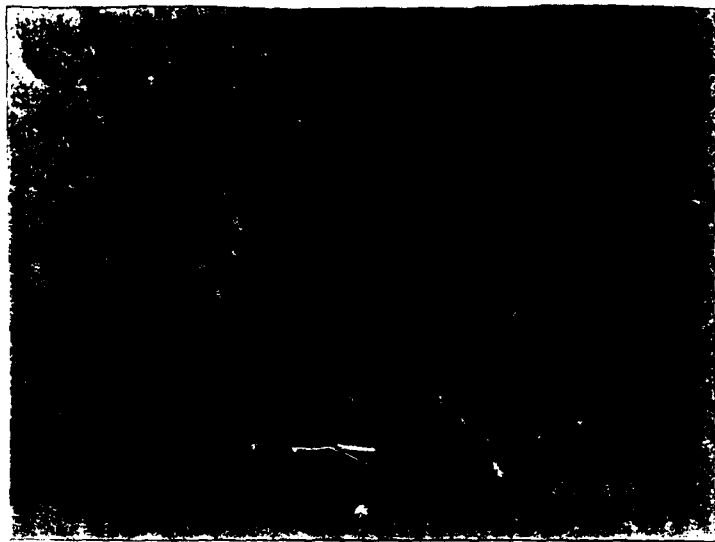


Figure 5: Dislocation network (InP:Fe) (Nomarski micrograph).



Figure 6: Faceting revealed by photoetching.

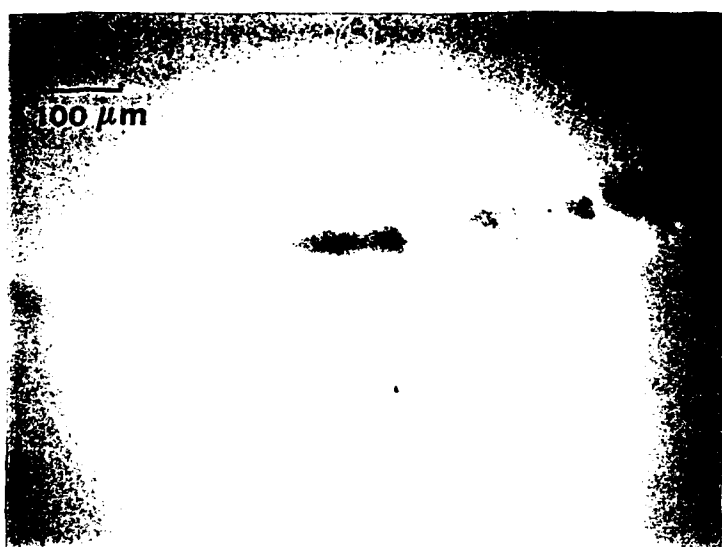
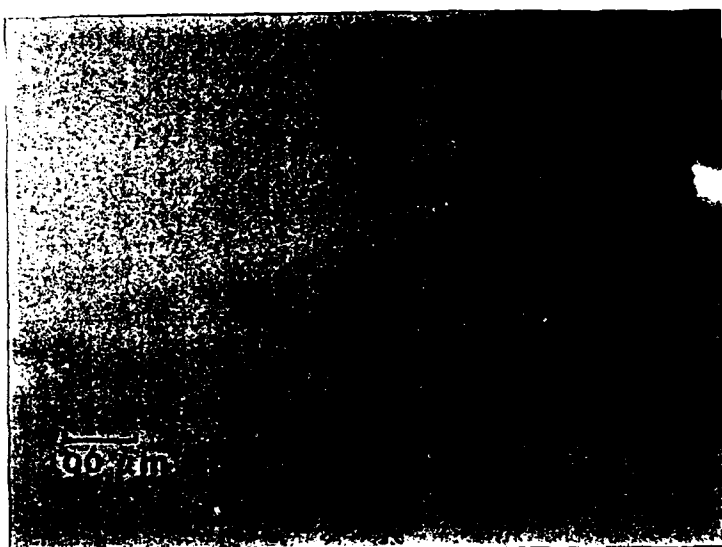
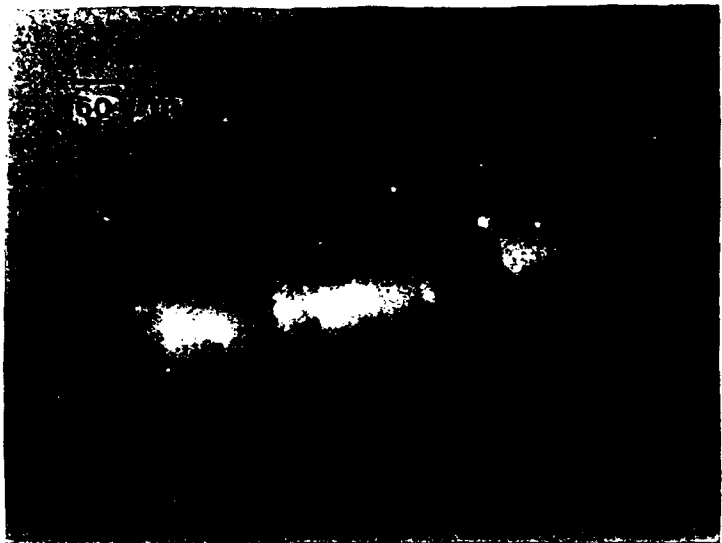


Figure 7: Twin lamellae (undoped n-InP) (Nomarski micrograph).

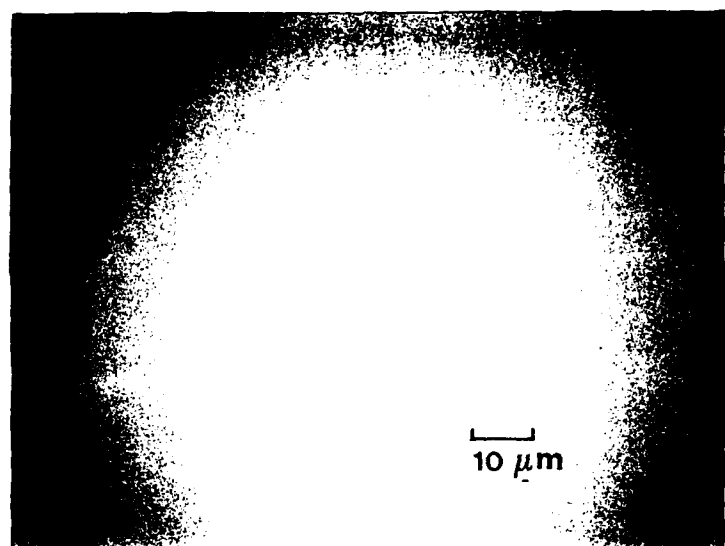


Figure 8: Twins (undoped n-InP) (Nomarski micrograph).

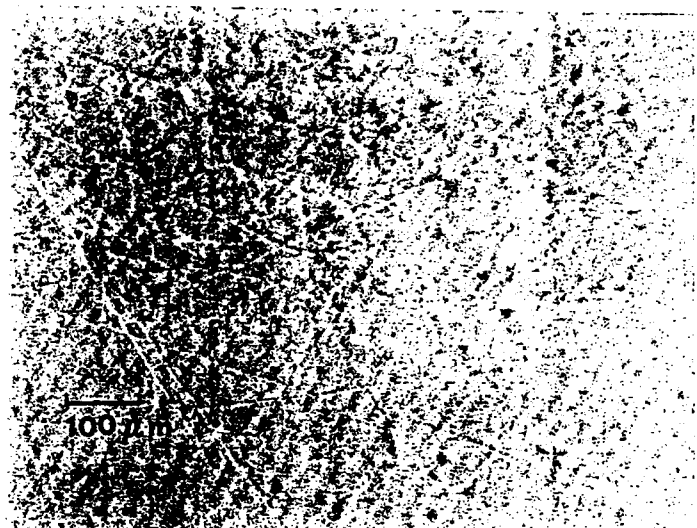


Figure 9: Subsurface damage (InP:Fe) (Nomarski micrograph).

Samples

Samples of different composition and supplied by different vendors were used for our research.

These samples are Semiconducting

n-type

Sn doped, $n \approx 5 \times 10^{18} \text{ cm}^{-3}$

S doped, $n \approx 2.2 \times 10^{18} \text{ cm}^{-3}$

supplied by Nippon Mining

undoped, $n \approx 10^{16} \text{ cm}^{-3}$

supplied by Rome Air Laboratory

p-type

Zn-doped, $p \approx 10^{18} \text{ cm}^{-3}$

p-type, Cd-doped, $p \approx 10^{17} \text{ cm}^{-3}$

Semiinsulating

Fe- doped

from different suppliers by MCP, Rome Air Laboratory, Sumitomo

CHEMICAL ETCHING AND MICROSCOPY OBSERVATION

Selective chemical photoetching was used as an auxiliary technique in order to reveal extended defects in InP the rate of etching is dependent on the crystallographic heterogeneities, such as dislocations, grain boundaries, twins or compositional non homogeneities, as microprecipitates and dopant growth striations (1,2). The etching procedure was the so-called DSL (Diluted Sirtl Mixture Applied with Light) (10,11) , which allows to reveal crystallographic and compositional defects. The morphology observations were carried out by optical microscopy (Nomarski) and PSM (Phase Stepping Microscopy) (12).

The DSL procedure consists of the chemical etching with a binary solution formed of CrO_3 and HF in water (10,11). The general composition of this mixture is labeled as $D_{1:x} S_a / b$ where each symbol denotes:

D 1:x the solution of one volume of S_a / b in x volumes of water

S_a / b is a solution formed of a and b volumes respectively of HF (48%) and CrO_3 (33%)

The 48% rich HF solution refers to weight concentration

The 33% rich CrO_3 solution is prepared by solving y gr. of CrO_3 on 2y gr. of water.

The main defects revealed can be summarized as :

Growth striations, mainly in semiinsulating material, these striations correspond to dopant fluctuations and should be studied on this report as related to short range fluctuations of the iron distribution in semiinsulating material, fig.4.

Grown in dislocations, fig.5.

Faceting, fig.6.

Twins both lamellar twins or presenting the shape of a microscopic inclusion are observed in the undoped n-type sample fig. 7 and fig.8. At both sides of the twin lamellae the crystal surface presents different roughness as revealed by the DSL etching fig. It will be complementarily studied with the Raman microprobe.

S-doped samples present a lower dislocation density, which is consistent with the better uniformity usually ascribed to the S-doped samples.

Some of the samples present a strong subsurface damage as a consequence of the polishing procedure, fig.9 ; this damage is only observed after chemical etching and cannot be appreciated after the mechanochemical polishing procedure in a first surface inspection.

RAMAN SPECTROSCOPY

Raman spectroscopy is a non destructive contact-less spectroscopic technique that provides a comprehensive structural and electronic understanding of semiconductor materials (13,14). Raman scattering can serve to gain information on crystal orientation, structural quality, composition of mixed crystals, dopant activation, carrier concentration

and so on... .

The main parameters to be analyzed in a first order Raman spectrum are:

- 1.- The intensity of the Raman peaks
- 2.- The frequency of the maxima
- 3.-The linewidth of the bands

The first order Raman spectrum of pure InP crystals (zinc blende structure) consists of an LO (Longitudinal Optic) and a doubly degenerated TO (Transverse Optic) modes; which are usually observed at 346 cm^{-1} and 304 cm^{-1} wavenumbers respectively (15). The allowance of these Raman peaks is governed by the Raman scattering selection rules, which for backscattering geometry are shown in table 1. Any deviation from these selection rules should be related to the existence of either disorder introduced by defects or local crystallographic misorientations. Besides, the above mentioned Raman parameters are strongly sensitive to the crystalline features of the material and are modified by the presence of defects, residual strain or crystalline damage (13,14).

In polar semiconductors, as InP, the free carrier plasma wave interacts with the longitudinal optical lattice vibrations, LO phonons, via their macroscopic electric fields (16,17). This coupling gives rise to an upper, L^+ , and a lower, L^- , branch of the coupled LO-phonon-plasmon modes instead of a pure plasmon and a pure phonon. The frequency at which the coupled modes are detected varies with the carrier concentration as far as the collision damping of the plasmon is small. These coupled modes allow to characterize different electronic parameters of the material, such as the carrier concentration and the mobility (18,19). On the other hand, the magnitude of the screening of the pure LO phonon allows to get an estimation of the surface depletion depth (20,21).

The use of a Raman microprobe allows to study all that features over micron size areas of the wafer surface (7, 18). The Raman scattering cross section of InP is quite small as compared to other semiconductors such as GaAs (22), which results in a very low scattering efficiency; therefore the acquisition of the Raman spectrum in InP is time consuming; which is specially true for microprobe analysis due to the small scattering volume. Usually in point illumination the laser power density is high enough to produce non equilibrium effects on the material with the corresponding influence they can have on

the Raman spectrum features.

All the wafers tested were cut perpendicularly to the (100) growth axis. All of them were studied as received from the supplier, mirror polished, and after chemical etching. The Raman spectra obtained on as received samples look different depending on the type of sample

~ **Type n and semiinsulating samples.** The Raman spectra obtained on these samples are characterized by a strong **forbidden TO peak and a weak LO peak** at 302 cm^{-1} and 346 cm^{-1} . The relative intensity of the LO and TO peaks in the undoped material depends strongly on the incident laser power density, which suggests the presence of a non negligible carrier photogeneration.

An anomalously strong **second order spectrum** (two phonon scattering processes: 2TO,LO+TO and 2LO) is observed between 600 and 700 cm^{-1} ; eventually it can be nearly as intense as the first order peaks in some of the studied specimens, fig. 10.

Besides these peaks characteristic of pure InP, two other spectral features are observed in these samples **a peak at 452 cm^{-1}** and a second one in the high energy wing of the LO peak **at approximately 350 cm^{-1}** . These peaks are usually observed in oxidized InP surfaces (23) and are due to solid phosphorus which is a product of the InP oxidation. The existence of these peaks in some of our specimens, that were not treated by any oxidation procedure gives evidence of a non negligible oxidation of polished (100) InP ambient atmosphere exposure.

p type samples.- Cd doped samples are characterized by a strong LO peak and a weak TO peak in agreement with the Raman scattering selection rules corresponding to an (100) surface. In addition, the presence of solid phosphorus does not clearly appear in the Raman spectrum and the intensity of the second order modes lies in the expected proportionality ratio as compared to the first order spectrum intensity $\approx 10\text{-}15$ times lower than the first order intensity (24).

The Zn-doped samples are characterized by a strong LO peak but also by the presence of solid phosphorus and high intensity second order spectrum, Figs 11 and 12. This sample

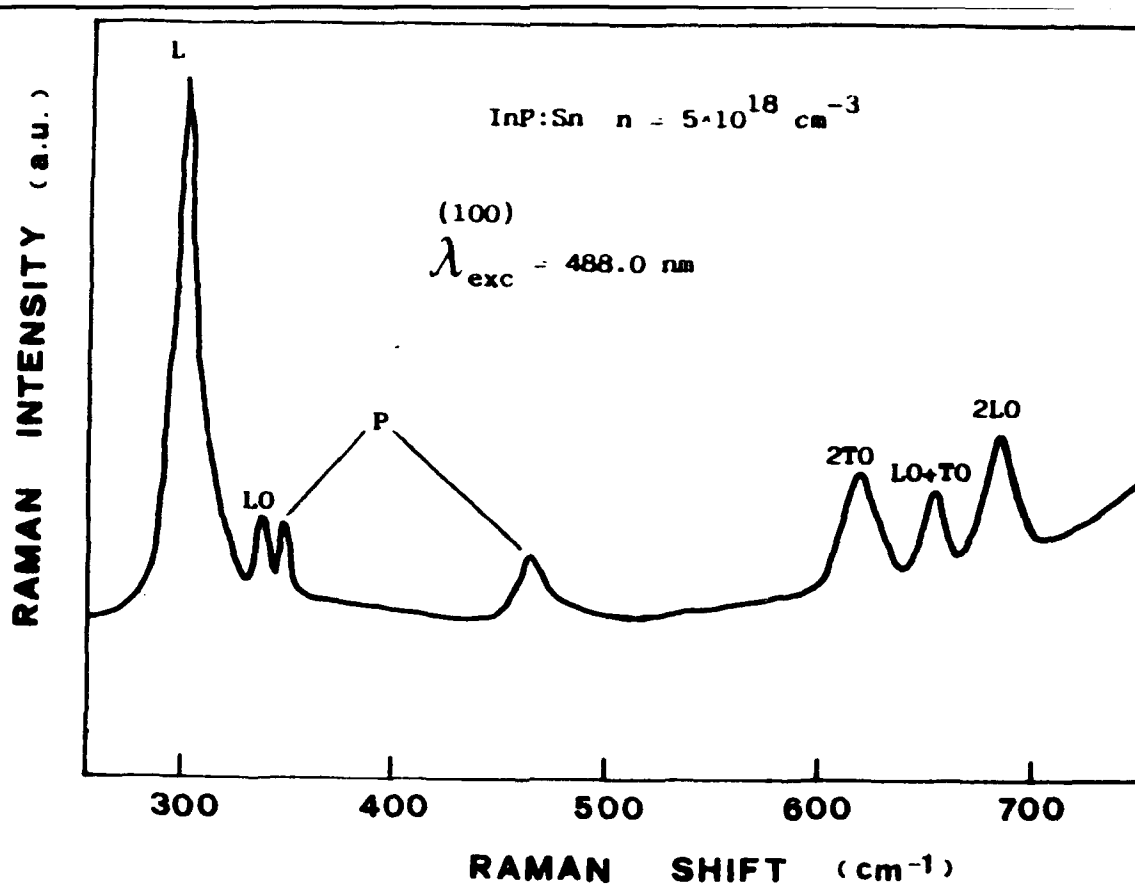
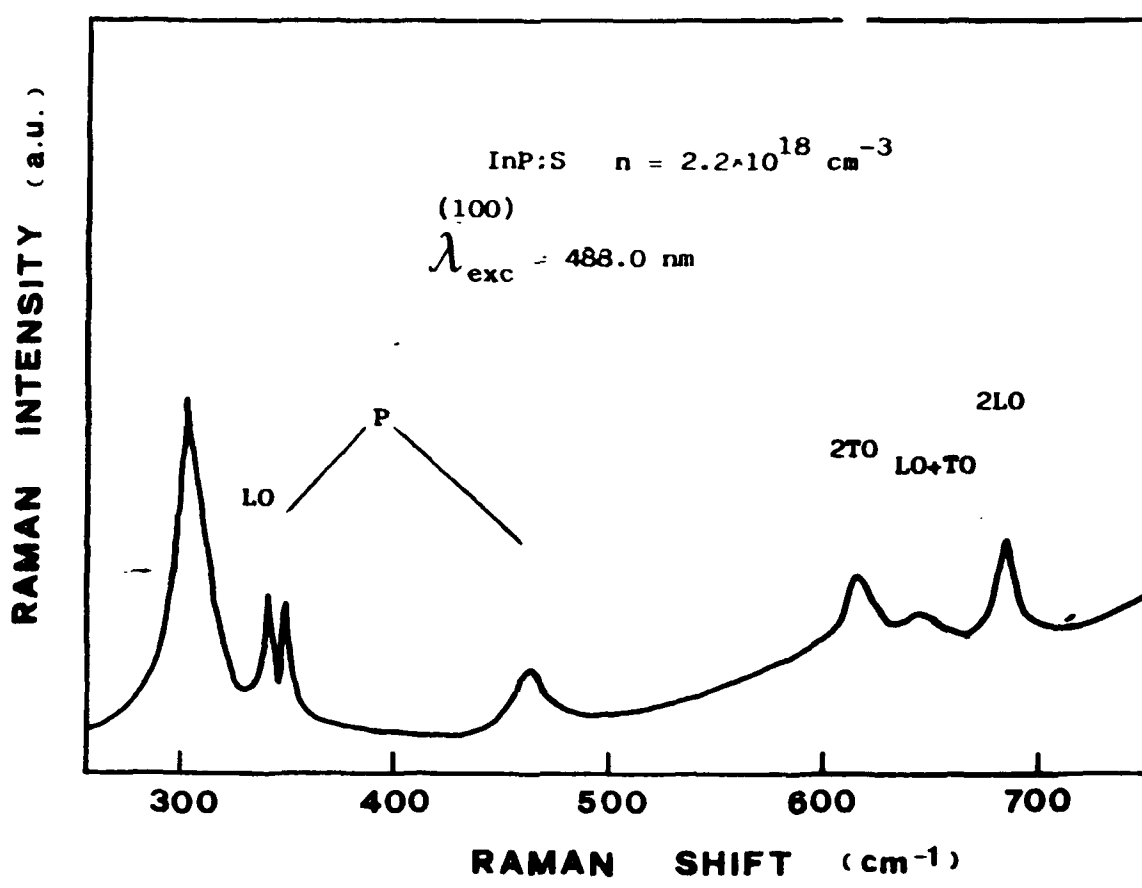


Figure 10: Raman spectra of InP:Sn and InP:S (100) (n-type).



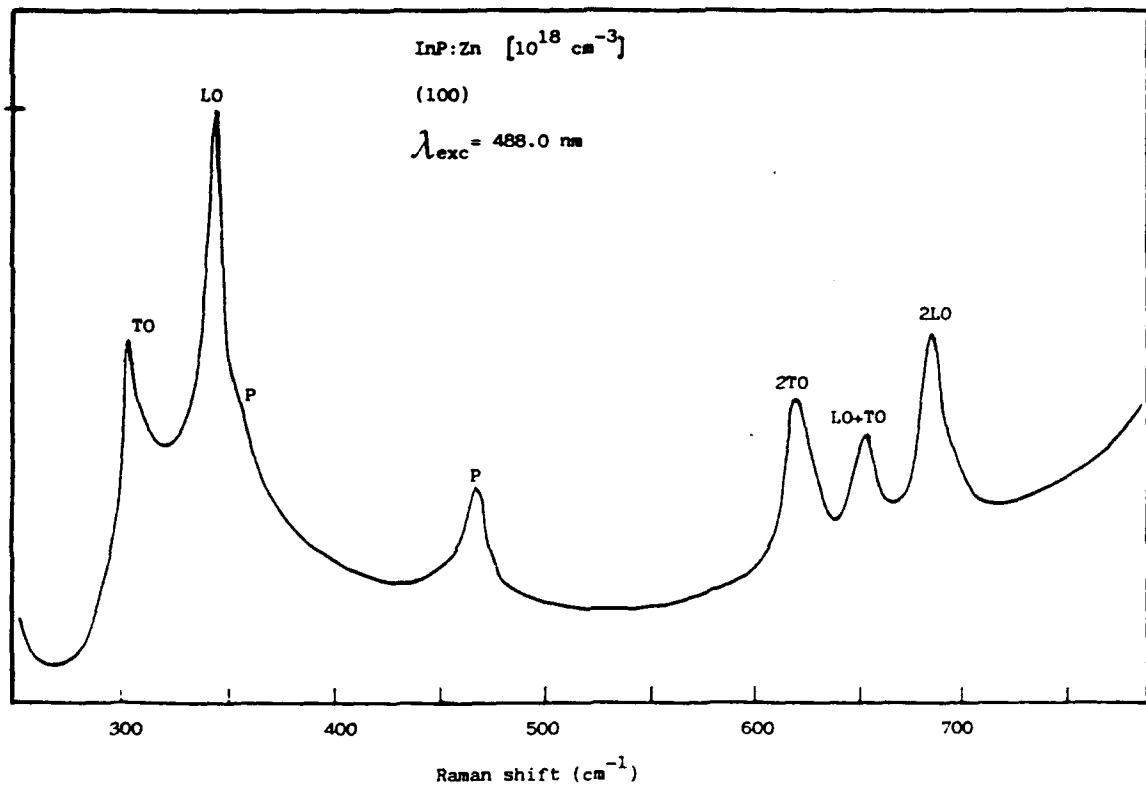


Figure 11: Raman spectrum of Zn doped InP (100) (p-type)

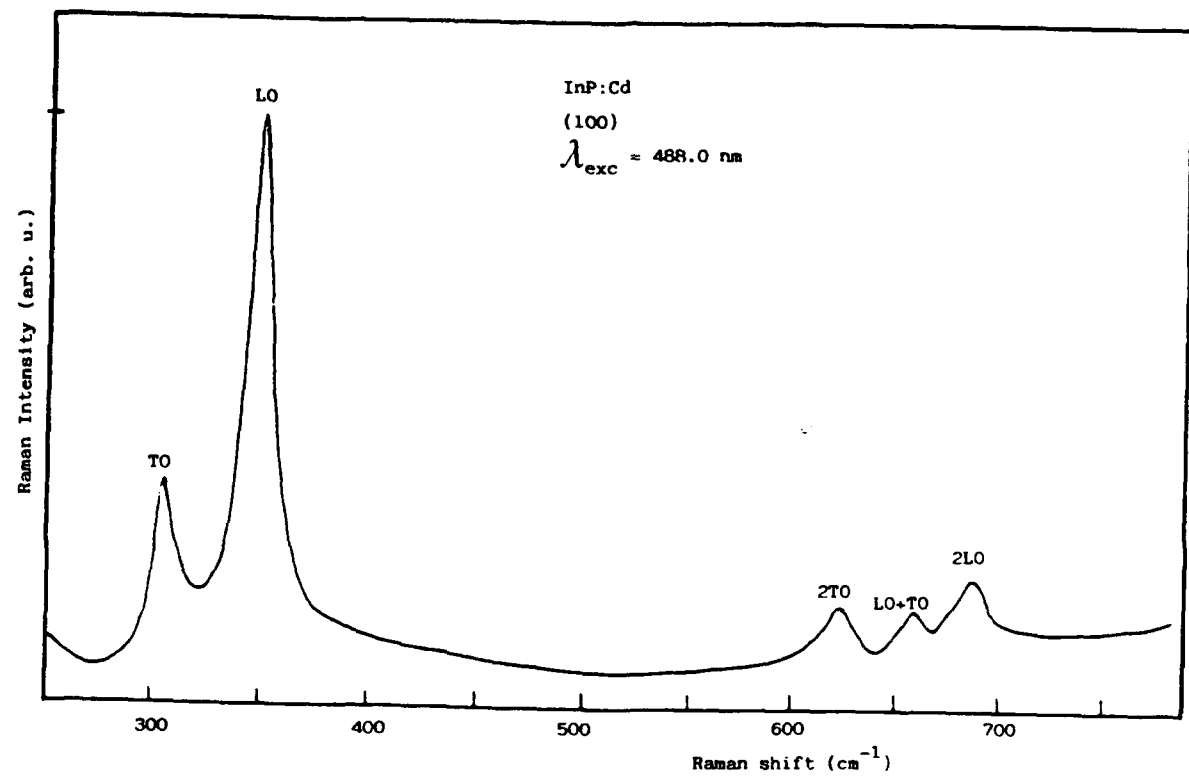


Figure 12: Raman spectrum of Cd doped InP (100) (p-type)

was long time stored in the laboratory.

These spectra are compared to those obtained on freshly **cleaved surfaces (110)** of the same samples, fig . In this surface the measured Raman spectra correspond to those expected from the selection rules, a **narrow TO peak ($\approx 5 \text{ cm}^{-1}$) at 304 cm^{-1}** and a **very weak LO peak**. The second order spectrum lies also on the expected intensity range according to the ratio between second and first order Raman cross sections. No vestiges of the 452 cm^{-1} and 350 cm^{-1} Raman structures, associated with solid phosphorus, were found in these cleaved surfaces.

Different hypothesis can be raised about the observed Raman spectra of our as polished surfaces.

1- The surface is damaged by the polishing procedure. The selection rule forbidden TO peak is then the result of the breaking down of the crystalline order. The polishing damage was studied by other authors (25,26), who showed that polishing induced damage produces a strong broadening of the LO Raman band.

2.- The surface is damaged due to the oxidation process, then it should be the result of the surface decomposition as it was reported to occur in GaAs (27)

3.-The forbidden TO peak is and L⁻ mode due to the presence of free carriers in enough high density, which in high resistivity material are generated by the laser beam and have a long lifetime due to the low recombination carrier efficiency in this material, that is known to have a very low surface recombination velocity (SRV) (28,29,30).

The last hypothesis is the most reliable for n-doped material, which has carrier concentrations above 10^{18} cm^{-3} , which would account for a considerable screening of the LO mode, giving an phonon-plasmon coupled L⁻ nearby the TO frequency. The Raman band is found at around 300 cm^{-1} , slightly below the TO frequency. On the other hand it is broadened in relation to the pure phonon mode, which supports again the L⁻ character of this band in our specimens.

The similarity between the spectra obtained for semiinsulating and n-type material would account for the fact that the spectrum of the semiinsulating material is due to the presence of intrinsic free carriers generated by the laser excitation. This hypothesis is confirmed by the fact that the TO like band is larger than that found for the freshly cleaved surface also

the maximum is found at lower frequency in a similar way as it was observed for the n type samples. On the other hand after chemical etching the first order Raman spectrum is not significantly changed in semiinsulating samples. This is not consisting with a TO mode allowed by damage or oxidation because an enough deep etching must remove either the damaged or the oxidized layers. In fact this is the consequence of the point illumination, that produces both long living photogenerated carriers due to the low surface recombination velocity and overheating; this last point is not critical in our experiments.

Another point of interest is the high intensity of the second order spectrum. This second order spectrum is strongly sensitive to the crystalline quality (31,32) being significantly reduced in damaged materials. Therefore it is rather improbable that the strong TO peak could be due to any lack of crystallinity. Finally, the difference with p type samples, that exhibit a Raman spectrum in agreement with the selection rules confirms that in both semiinsulating and n type materials the Raman spectrum is dominated by the coupling between collective free carrier oscillations and LO phonons. In semiinsulating material the high carrier concentration producing the coupling with the longitudinal optical phonons is produced by the laser excitation and the high intrinsic carrier concentration estimated from the coupled plasmon modes is the consequence of the very low surface recombination velocity in semiinsulating InP; the Raman spectrum strongly depends on the incident laser power density; which is consistent with the above description.

We have studied the intrinsic carrier generation in different samples characterized by different surface morphology, as revealed by the selective DSL photoetching procedure. These revelations are characterized by:

Conspicuous growth striations, fig.13.

High EPD, fig.14.

Low EPD, fig.15.

Strong subsurface damage, fig.16.

The influence it has on the spectrum and on the intrinsic carrier generation is estimated in the calculated electron concentration. The excitation was performed at different incident laser power densities. The carrier generation as expected is limited by the dislocations and

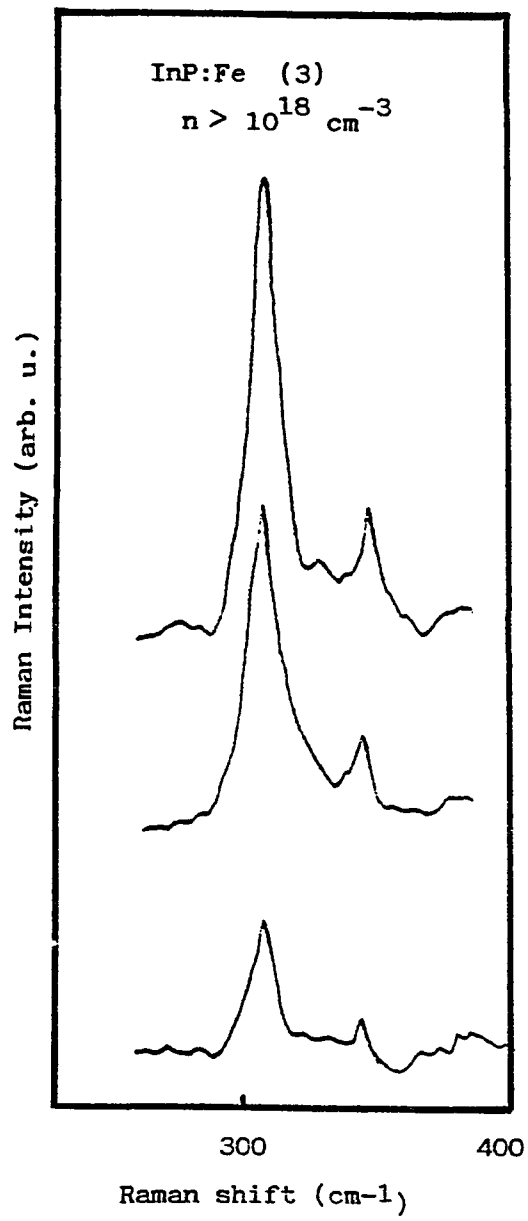


Figure 13: Raman spectra of semiinsulating InP:Fe obtained for different incident laser power densities on an (100) surface showing strong growth striations after chemical etching.

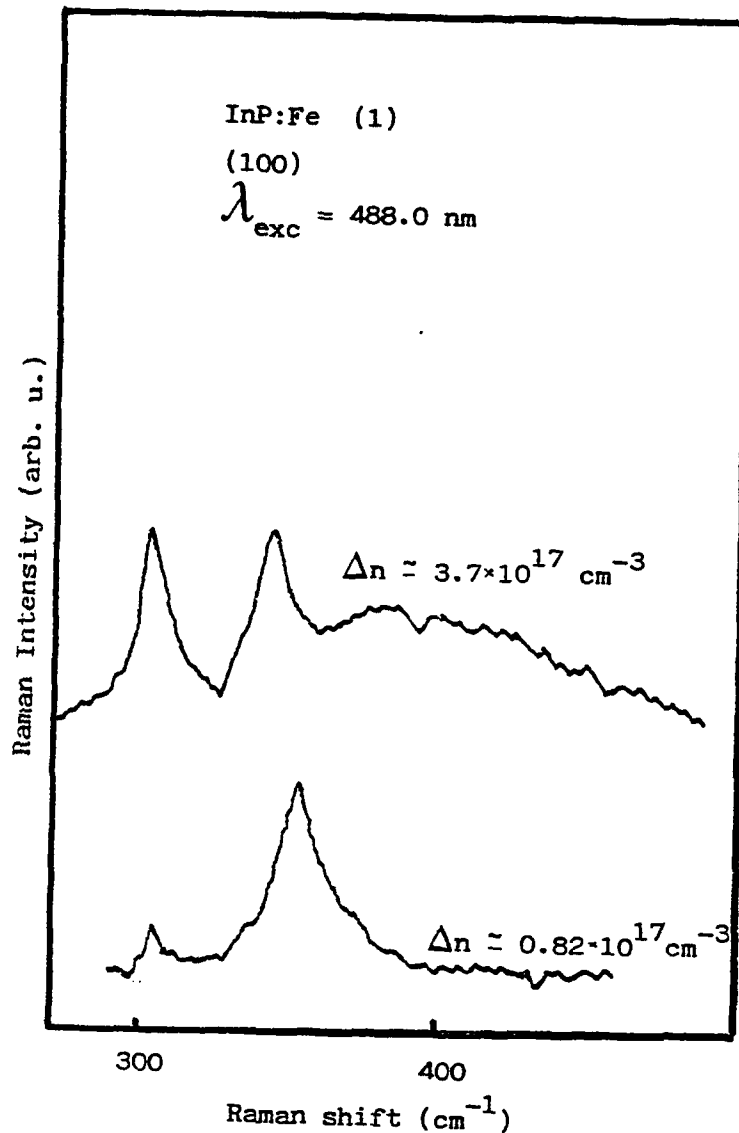


Figure 14: Raman spectra of semiinsulating InP:Fe obtained for different incident laser power densities on an (100) surface with high dislocation density.

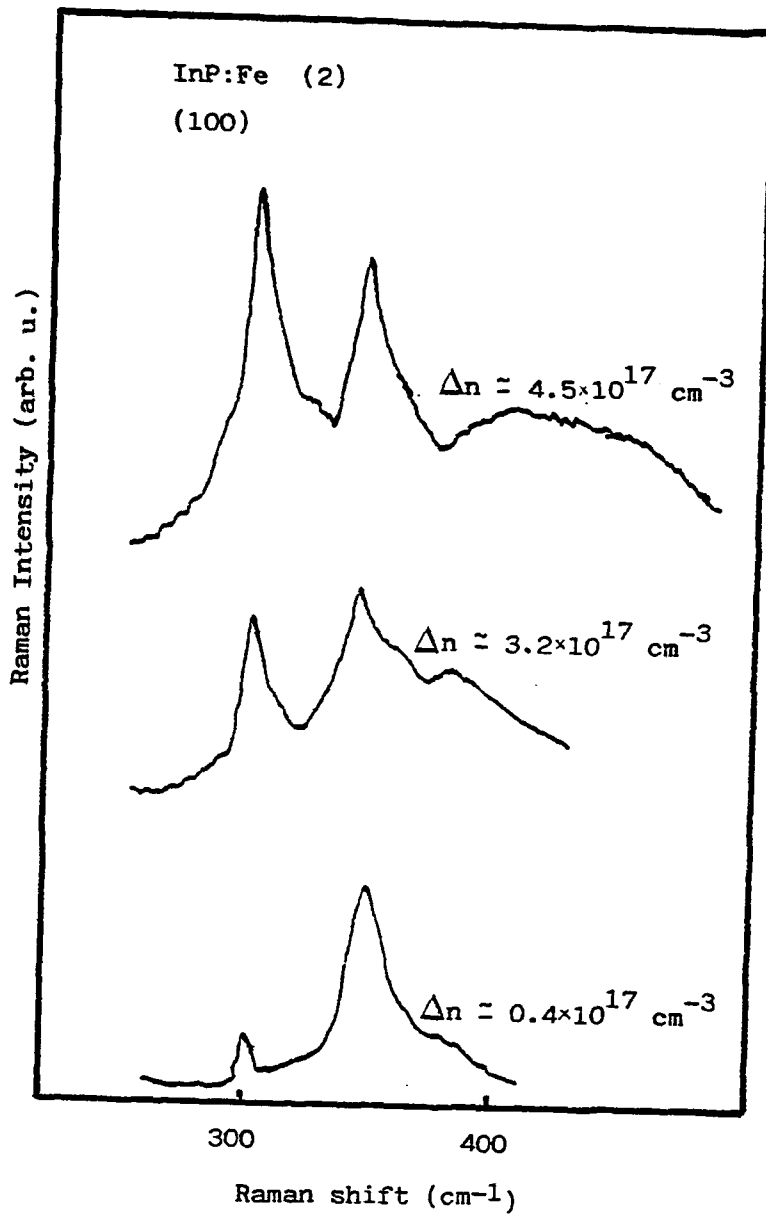


Figure 15: Raman spectra of semiinsulating InP:Fe obtained for different incident laser power densities on an (100) surface with low dislocation density.

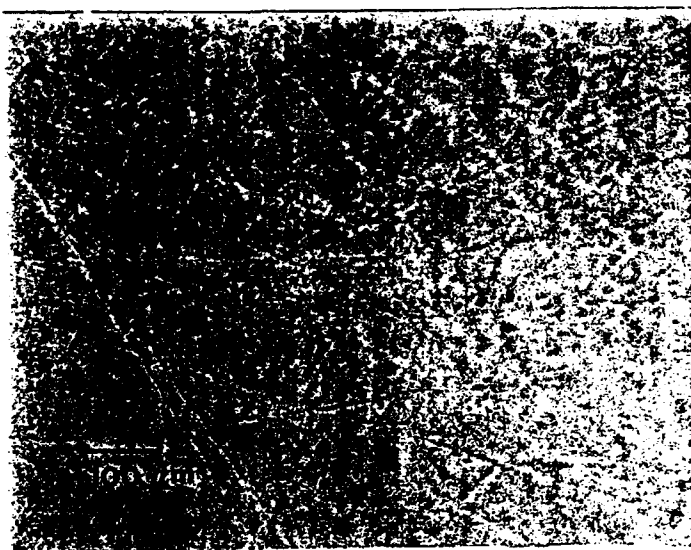
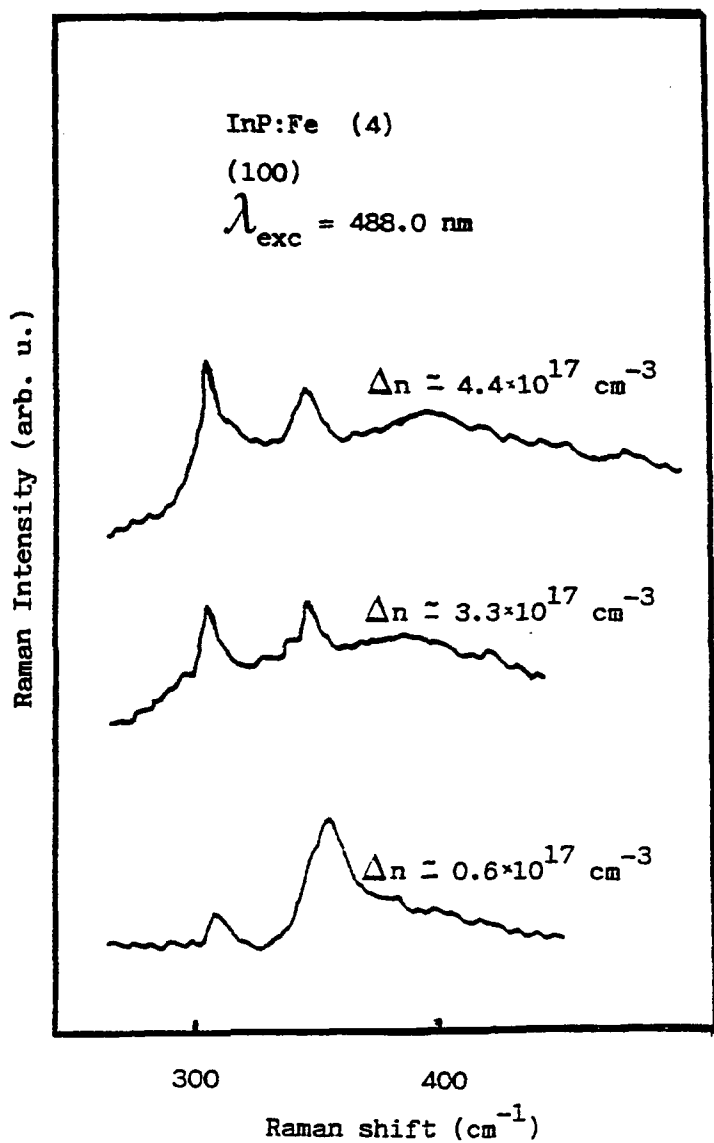


Figure 16: Raman spectra of semiinsulating InP:Fe obtained for different incident laser power densities on an (100) surface with subsurface damage.

the subsurface damage, through changes in the recombination efficiency.

Second order spectrum

The second order Raman scattering is a two phonon process. In InP the analyzed second order spectrum consists of three Raman peaks at 622 cm^{-1} , 655 cm^{-1} and 688 cm^{-1} , that correspond to the combination of two zone center phonons, 2 TO, LO+TO and 2 LO respectively (24).

The second order spectrum is strongly sensitive to the crystal quality, when damage is present in the probed volume its intensity decays (31,32). The second order spectrum recorded in a polished sample is very high, which confirms that the crystalline quality was not perturbed by the polishing procedure. This rules out the hypothesis of a highly damaged surface as a consequence of the oxidation and the polishing procedure, confirming thus the previous discussion about the origin of the Raman spectra in a polished samples.

Another important point to be considered is the significant decrease of the second order intensity in the chemically etched samples, fig.17. This decrease is observed together with the decrease of the 452 cm^{-1} and 350 cm^{-1} Raman bands related to solid phosphorus issued of the oxidation. In this context the most reliable hypothesis about the high intensity of the second order is a band bending effect. The second order spectrum presents a very sharp resonance peak near the E_1 gap of InP (24). This resonance is much sharper than that of the first order spectrum. Therefore the high intensity of the second order can be interpreted in terms of an enhanced resonance due to band bending as a consequence of the oxidation, probably at the interface between solid phosphorus and InP. It should be remembered that both the second order peaks and the solid phosphorus are progressively reduced by the chemical etching and are not observed in freshly cleaved surfaces and in Cd doped p type InP (3,4).

Another proof is provided by the correlation between the intensity of the solid phosphorus related peaks and the intensity of the second order peaks which is represented in fig.18 for n-type Sn-doped and semiinsulating materials respectively. In these plots the correlation between the second order intensity and the solid phosphorus peaks appears unambiguously, which calls for the influence that an oxidized surface can have on the interface electronic properties via band bending effects.

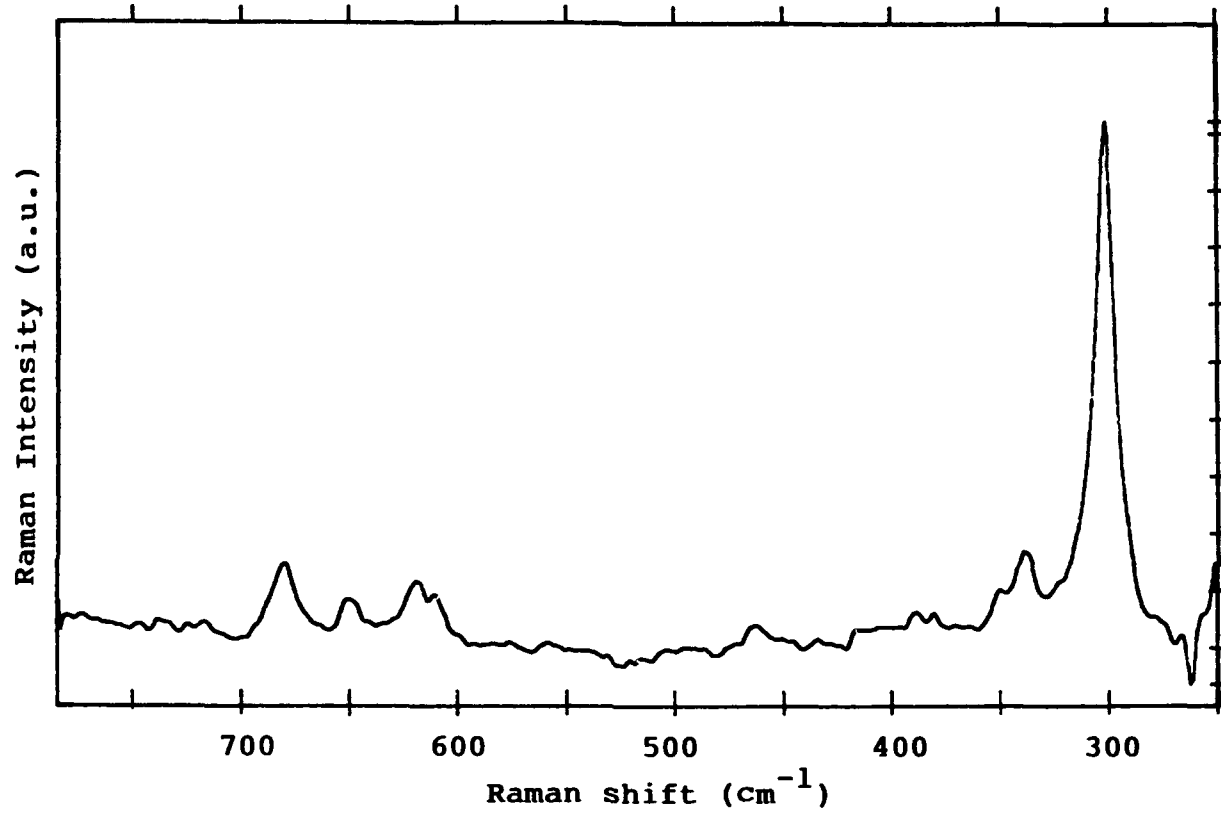


Figure 17: Raman spectrum of (100) InP:Fe chemically etched (DSL)

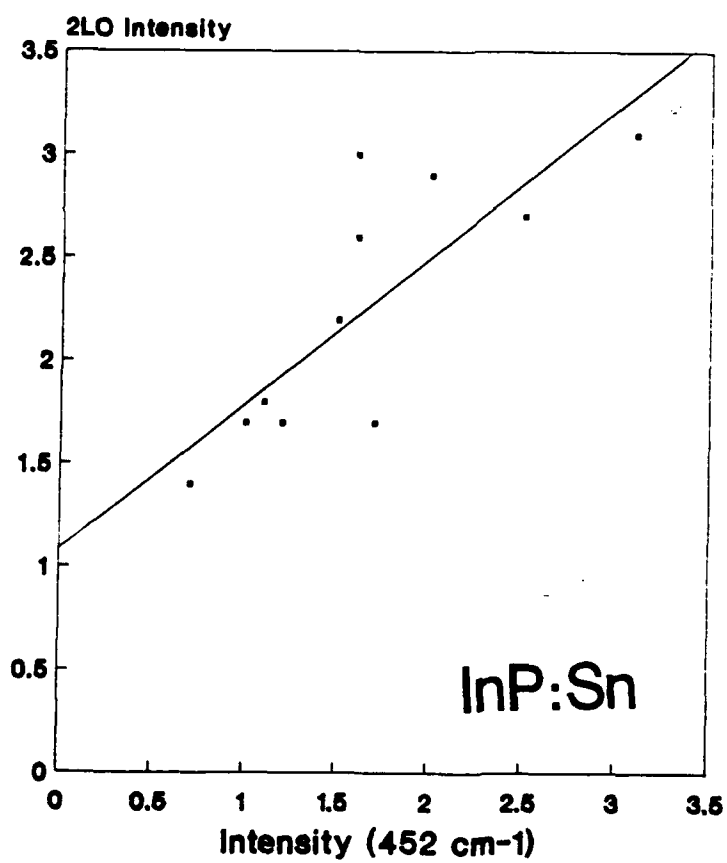
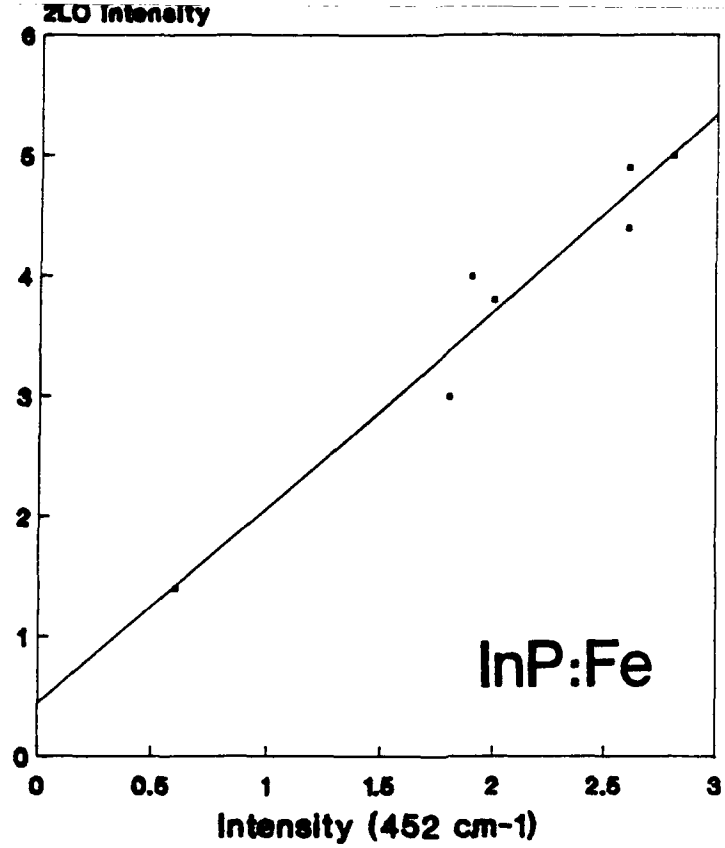


Figure 18: Correlation between the intensity of the 452 cm^{-1} solid phosphorous Raman peak and the intensity the second order peaks in InP:Fe and InP:Sn.

Oxidation efficiency is apparently dependent on both the dopant and the treatment undergone by the samples. Anyway, systematic intentioned oxidations on different samples would be necessary in order to argue about the influence of doping in the oxidation. What can be concluded is that InP can be considerably oxidized under ambient exposure.

Homogeneity

An essential point of our work is devoted to the homogeneity of InP wafers at both microscopic and macroscopic range. From the point of view of the Raman measurements different sources of non homogeneity are:

Crystallographic defects

Inhomogeneous oxidation

Inhomogeneous doping

The samples were rastered with the Raman microprobe in order to determine the evolution of the Raman spectrum across the wafer diameter, for the assessment of the long range homogeneity, or along lines crossing extended defects, for the short range homogeneity.

In the case of the oxidized samples the intensity of the second order spectrum was found to be non uniform across a wafer diameter, the intensity of the solid phosphorus Raman peaks was found to follow a similar non uniformity. In other words the oxidation can be a source of non homogeneity of the InP surfaces. This is shown in figs. 19 and 20, where several of these Raman parameters are represented across an $<110>$ diameter of different wafers.

Different Raman parameters were represented as obtained point by point across an $<110>$ scanning line. It was shown that Sn-doped is significantly more inhomogeneous than S-doped samples, fig. 21. It should be noted that the line broadening of the L^- band is due to the q-rule relaxation due to scattering by ionized impurities. Apparently this effect is much conspicuous in Sn-doped samples, and it presents a more inhomogeneous distribution than S-doped wafer, which is consistent with the usually claimed good

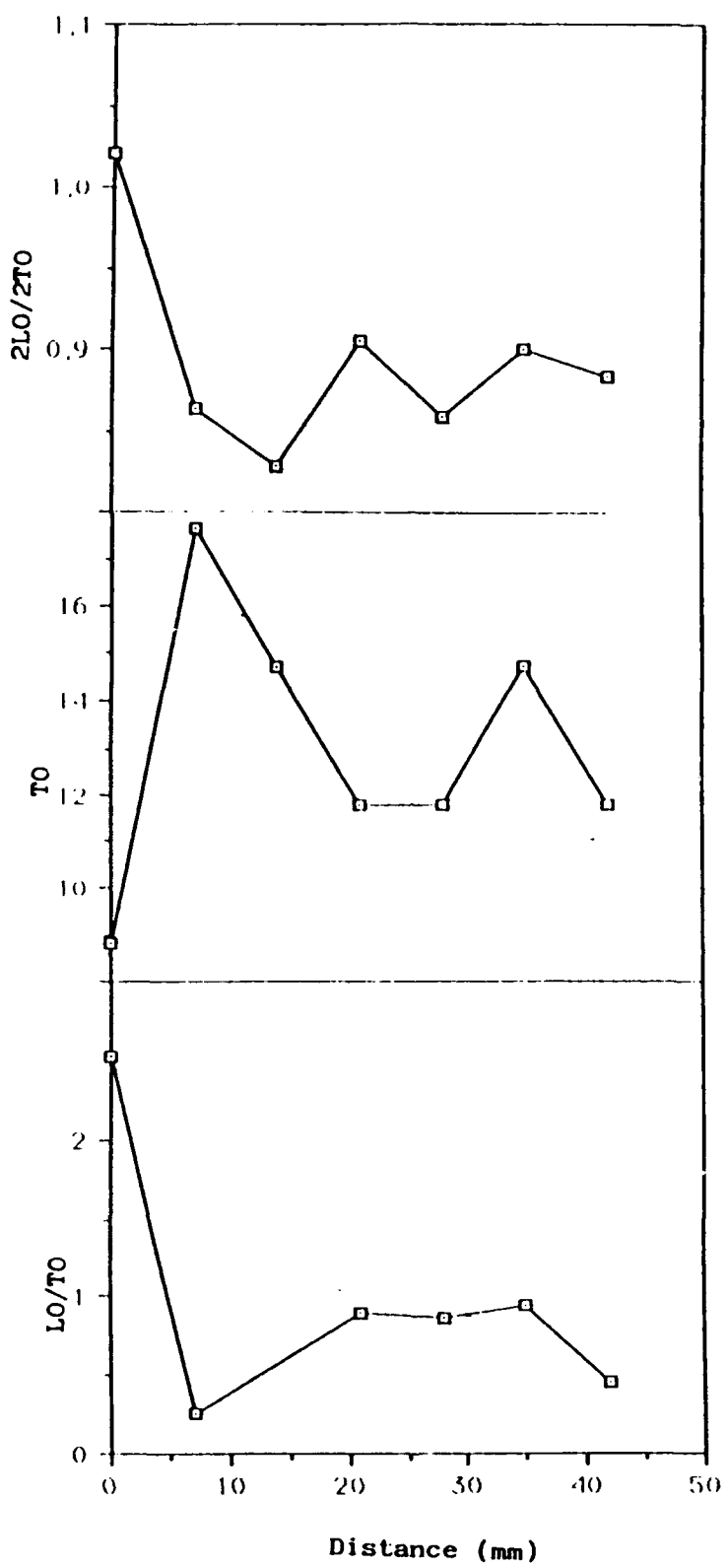


Figure 19: Study of the homogeneity in InP:Sn. Different Raman parameters are represented as a function of the position across an $<110>$ diameter of an (100) wafer

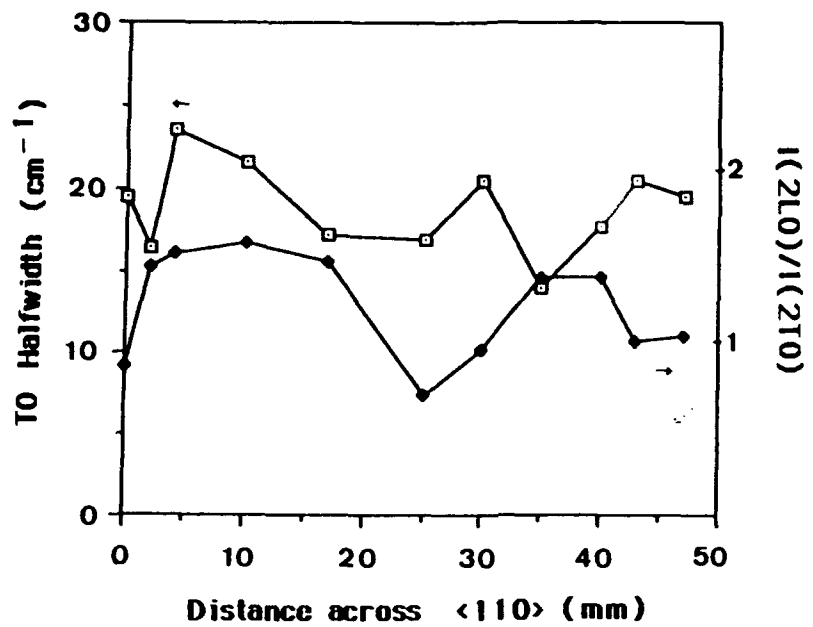


Figure 20: Study of the homogeneity in InP:Fe. Different Raman parameters are represented as a function of the position across an $\langle 110 \rangle$ diameter of an (100) wafer

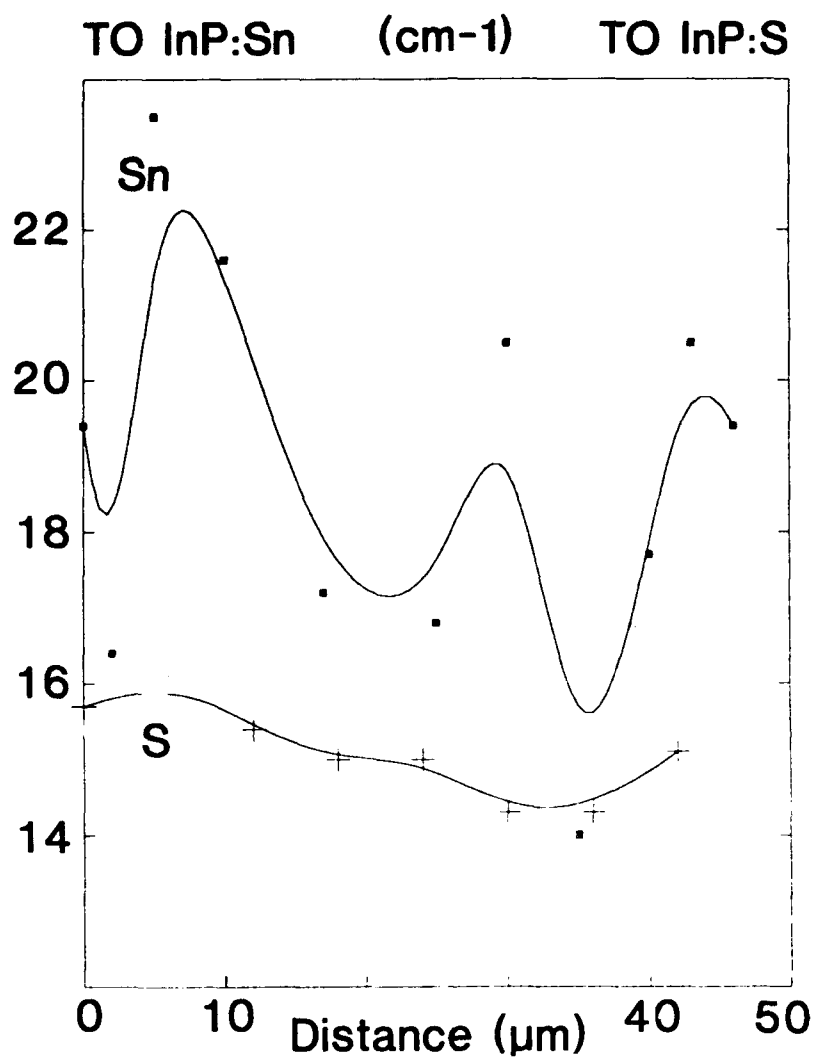


Figure 21: TO width across and <110> diameter for InP:Sn and InP:S wafers.

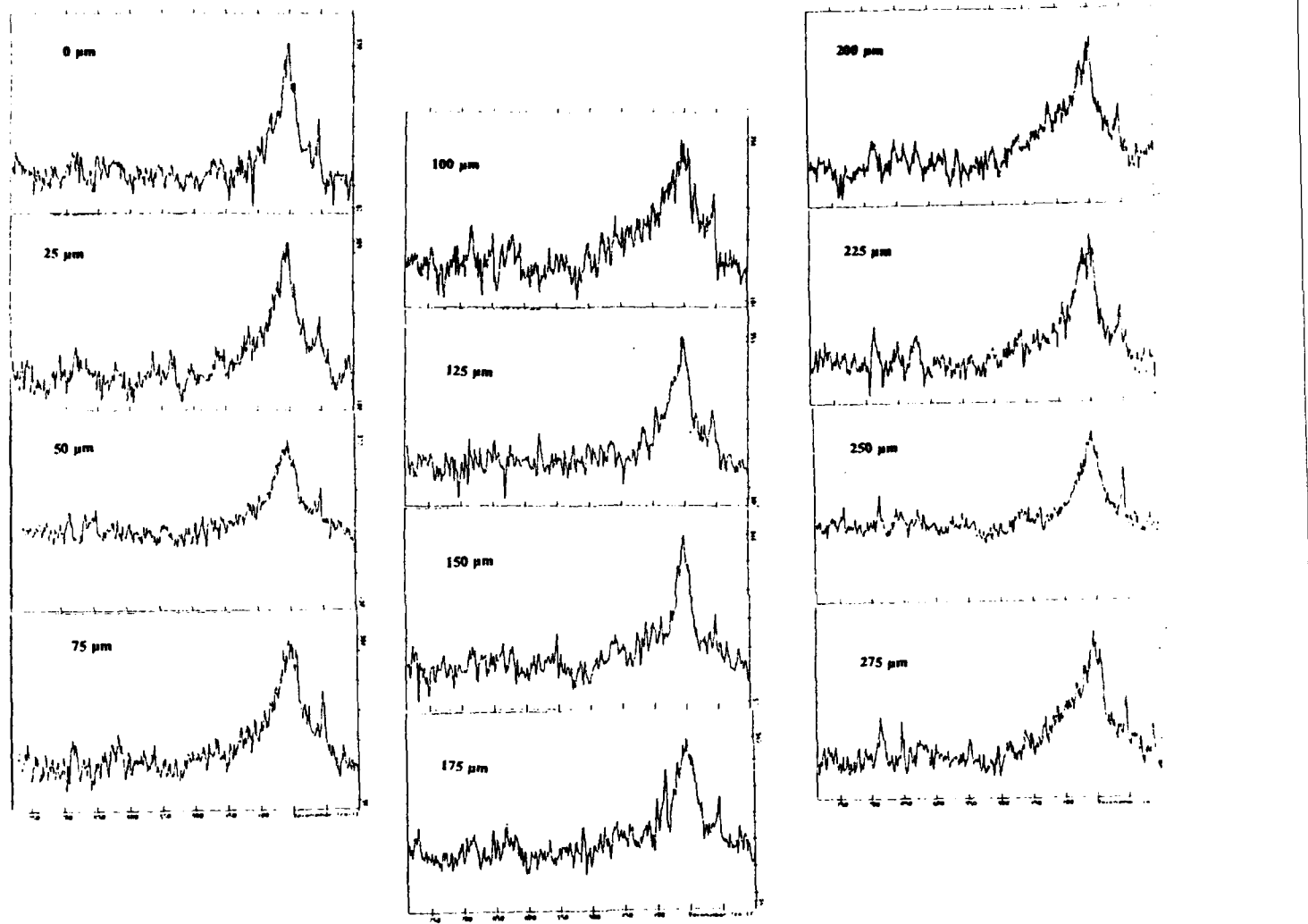


Figure 22: Raman spectra obtained along a scanning line, crossing the growth striation pattern in InP:Fe.

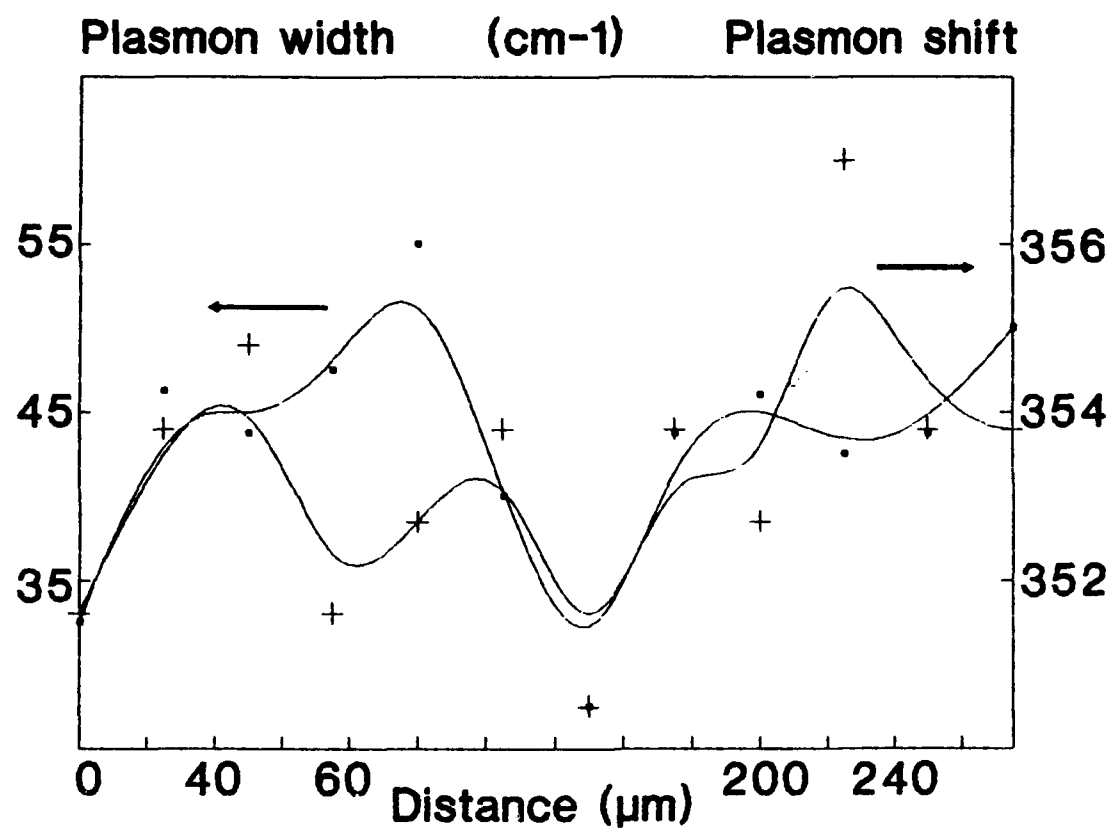


Figure 23: Plasmon width and frequency obtained from the spectra of fig 20.

homogeneity of S-doped InP.

Growth Striations

Iron doping presents inhomogeneities that are associated with density fluctuations (33,34). Iron-doped samples are compensated giving an equilibrium electron concentration of 10^8 cm^{-3} , which is well below the limit expected for screening the LO phonon. Nevertheless the Raman spectra obtained in these specimens reveal the presence of phonon plasmon coupled modes that can be associated with carrier photogeneration; the series of Raman spectra obtained along a line crossing transversally the growth striations are shown in fig.22. In this context the fluctuations observed in the LO linewidth and frequency, fig.23, can be associated with fluctuations of the Fe^{2+} content, which is an active recombination center limiting the lifetime of the photogenerated carriers. The fluctuations herein measured correspond to about 3-4 % and a period of 50 μm , which seem to account for the doping growth striations typical of the Fe doping in InP. This proves that they can be revealed in Raman scattering by means of the intrinsic photoexcited carriers, assuming that there are not changes in the surface recombination velocity.

Extended Defects

The study of the crystallographic defects was devoted to the determination of the structural characteristics of the chemically revealed defects by means of the Raman microprobe. Among the most common crystallographic defect in InP are twins. We present herein the study of twin lamellae in undoped n-type material grown by Rome Air Laboratory. This wafer was characterized by a well defined twin lamellae. Twin lamellae are early revealed by mechanochemical polishing. The lamellae crosses the wafer oriented parallel to the $\langle 110 \rangle$ axis on (100) planes. A clear revelation of this 140 μm large twin lamellae was achieved after DSL (Diluted Sirtl Mixture Applied with Light) photoetching (10,11), fig.24. Prolonged photoetching reveals a non homogeneous morphology at the twin exposed areas. An optical microscopy (Nomarski) inspection of the surface morphology after photoetching at both sides in which the wafer is divided by the twin lamellae reveals a different etching pattern from each other, fig.25. On one side the density of revealed defects is low, while on the other side a markedly irregular surface is

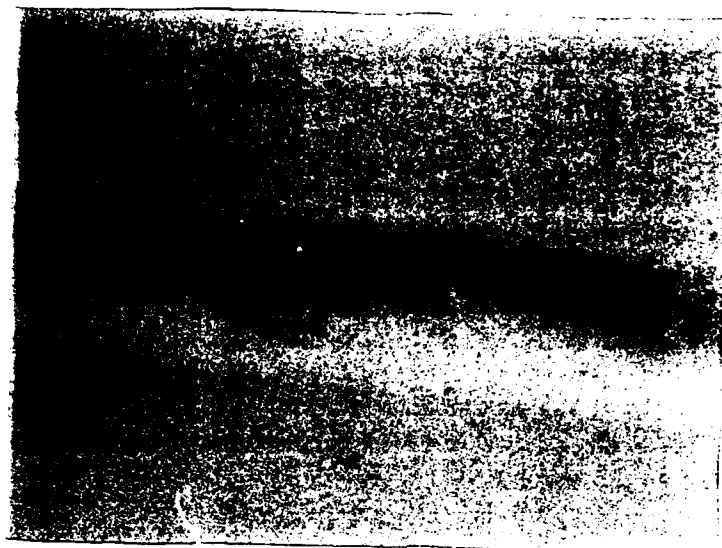


Figure 24: Nomarski micrograph of the $\langle 110 \rangle$ aligned twin lamellae revealed by DSL.



Figure 25: Nomarski micrograph after photoetching of the polycrystalline side of the wafer.

observed. This reveals a strongly inhomogeneous etching rate in this faceted area, which is the result of a highly non-uniform defect distribution (10,11).

This is confirmed by the Nomarski observation of the cleaved plane (110) crossing the twin, cleavage was done in air. A region of this plane exhibits a flat and clean surface, while the other region presents an irregular surface, with well revealed growth striations. The first of these regions is observed far from the twin, while near the twin area the cleaved surface shows contrasted growth striations. Faceting is clearly observed at the twin planes and in the regions surrounding the twin, the growth striations are bent crossing nearly transversally the twin, fig.6. All that reveals that the liquid-solid interface was really irregular in this volume, which should result in a strongly non uniform growth rate. It should be noted that far from the twin on the perfect side of the wafer the cleaved surface is flat and inhomogeneous growth cannot be appreciated. Faceting is usually associated with chemical inhomogeneity. All that should reveal that the crystal has two regions with different chemical composition. Taking into account that the crystal is undoped it is rather probable that deviations from the stoichiometry could be at the origin of this faceting and twining.

The photoetching depth was measured by PSM (Phase Stepping Microscopy) (12). The etching rate at the exposed twin surface is shown to be smaller than the etching rate in the matrix, fig.26. The exposed surface of this kind of twin on (100) plane is (221). While in the cleavage plane crossing the twin the (110) surface is exposed for both the matrix and the twin. This suggests that the differences in the etching rate are rather probably due to the orientational factor. Nevertheless, the observation of non uniform photoetching in twinned areas seems to claim for a defect influence on the photoetching rate in addition to the orientational factor. The prominent areas, which are characterized by slower etching rates are usually considered with higher donor concentration, herewith more n-type carriers are expected in these regions.

Typical Raman spectra obtained at different points of the scanning line are shown in fig.27.

The spectrum measured in the (100) plane of the matrix presents an LO-like peak and a weak TO peak. In the (221) exposed plan of the twin the TO peak is observed, the LO

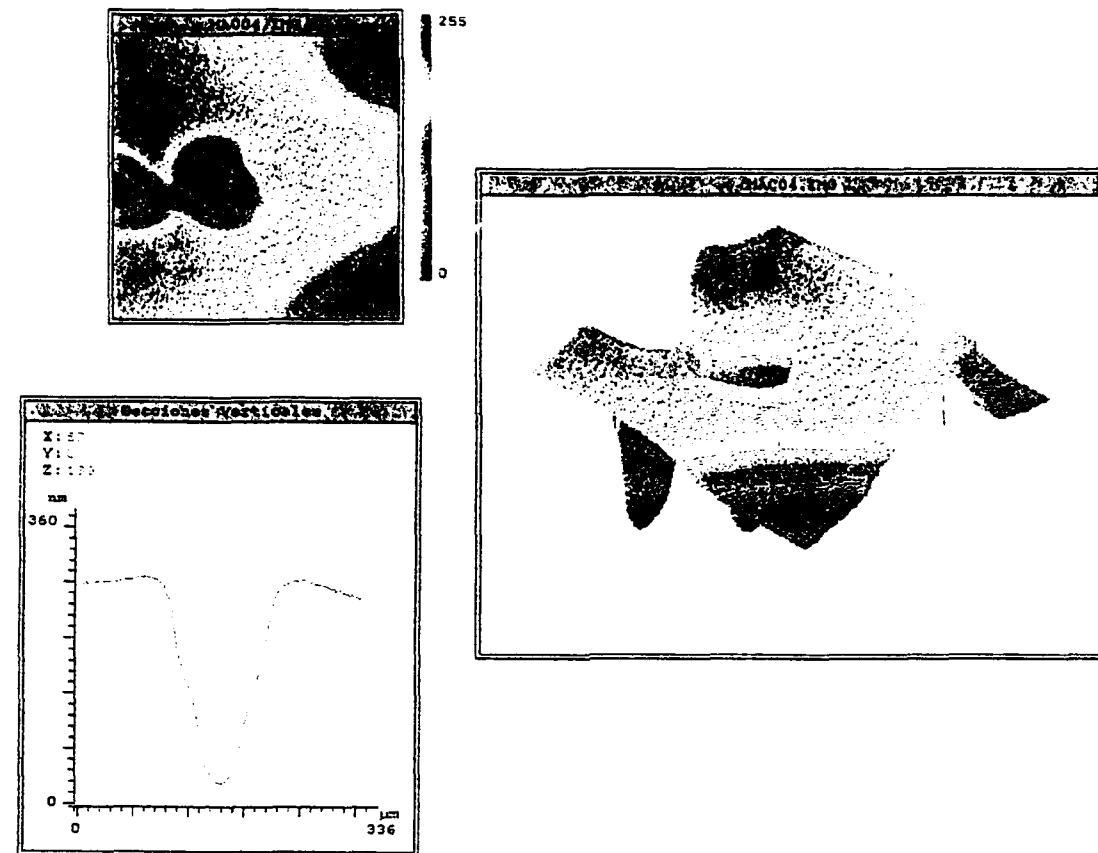
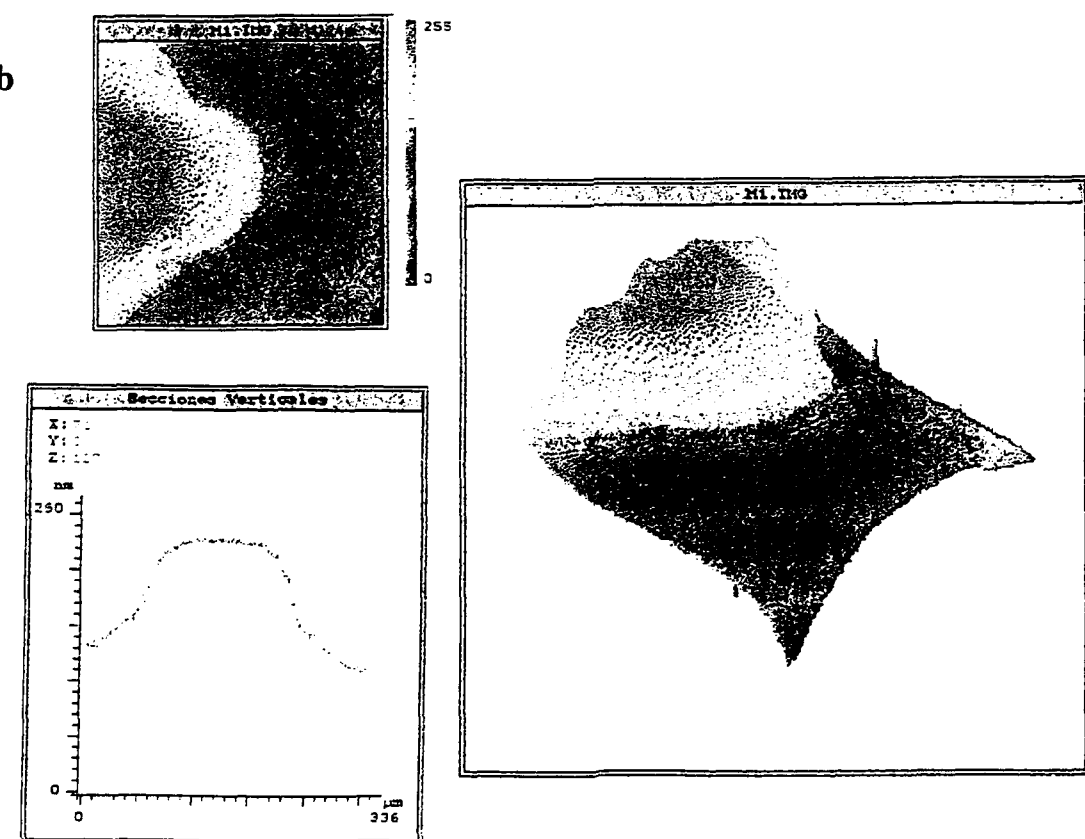


Fig.26.-a) 2D and 3D images of the photoetched polycrystalline area obtained by PSM (Phase Stepping Microscopy) and a z axis profile showing a deep depression.
b) 2D and 3D images of the twin lamellae parallel to the $\langle 110 \rangle$ crystal axis and z axis profile showing the typical photoetch profile.



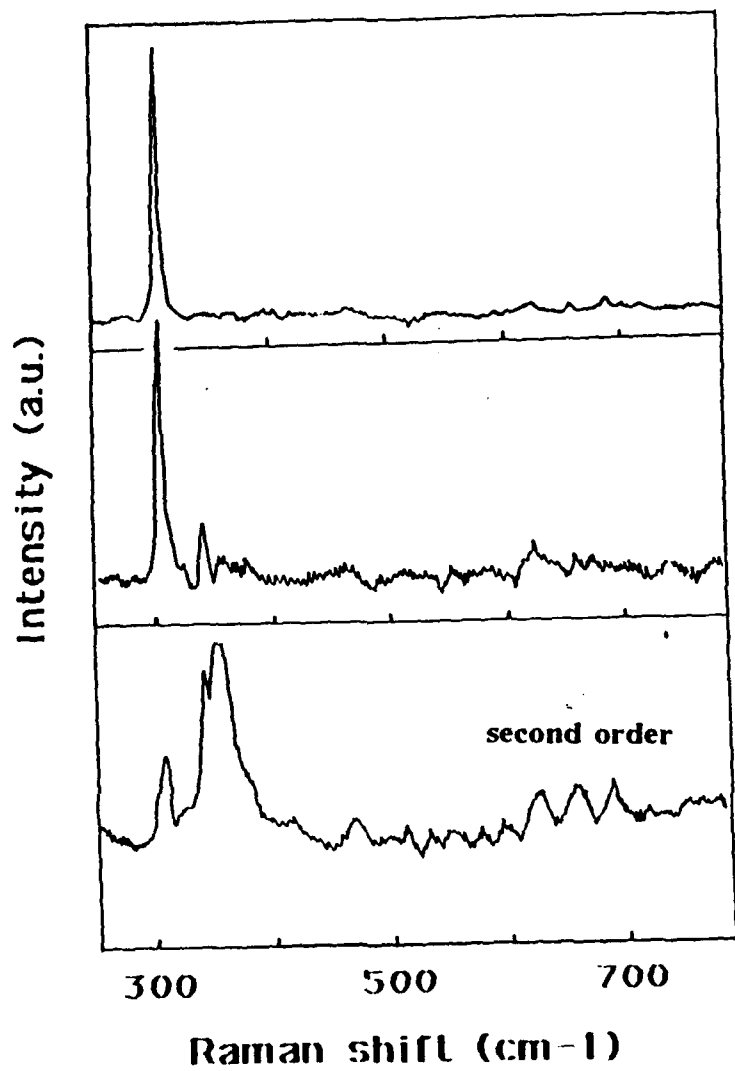


Figure 27: Raman spectra obtained at different points of the scanning line crossing transversally the twin lamellae.

mode is weak in this area. In the cleaved surface the only peak allowed is the TO which is seen for both the matrix and the twin, as expected for (110) planes in backscattering configuration.

Now special attention will be paid to the Raman spectra measured in the regions neighboring the matrix- twin boundary, for which the LO mode is allowed. The LO band measured is larger than that expected for a phonon-like Raman peak. It has been reported that strain can produce anomalous broadening of this Raman band (24). An alternative hypothesis is a coupling between the LO phonon and the collective excitations of free carriers (16,17). As it was mentioned above this coupling will give two bands, the so-called L^+ and L^- coupled phonon plasmon modes, which shift from LO to the plasma frequency and from 0 to TO respectively for increasing carrier concentration. Then it is rather probable that the observed broad LO-phonon band would be due to an L^+ plasmon overlapping the allowed LO phonon. The wafer was nominally undoped n-type and the average electron concentration was around a few 10^{16} cm^{-3} . For such an electron concentration the L^+ mode is phonon like and coincides with the LO phonon band. Therefore the observed plasmon-like band observed shall be the consequence of intrinsic carrier generation, which is available in our experimental conditions, due to the low surface recombination velocity characterizing n-type InP (28,29).

This was confirmed by Raman measurements performed with increasing laser power density, for which the plasmon-like character of the LO-like band is enhanced as more intrinsic carriers are available. As it was above mentioned the Raman efficiency is very weak, taking into account the small probed volume a compromise between laser power density and measurable Raman intensity leads to intrinsic carrier generation, which is not removed because of the low surface recombination velocity in n-type InP.

The Raman spectrum was measured at several points along a line crossing the twin lamellae for different laser power densities. The main spectral features observed in these measurements were the LO broadening and backward frequency shift for increasing incident laser power, fig.28. Furthermore, this effect is not uniform along the scanned line but becomes more intense as the twin edge is approached. This last observation suggests that the carrier recombination efficiency is reduced in such areas as compared to the matrix. On the other hand the dependence of the frequency shift with the laser power

density confirms that the main contribution to the LO frequency shift and broadening comes from the generation of photocarriers and not from residual strain due to modified bonding in such areas; which on the other hand cannot be neglected and will be discussed later in relation to the TO phonon mode analysis. According to the frequency shift of the L⁺ band the photogenerated electron concentration for the laser power densities used was in the 10¹⁶-10¹⁷ cm⁻³ range depending on the zones probed, up to ten times above the equilibrium carrier concentration.

The intrinsic photogenerated carrier lifetime is limited by either the surface recombination velocity or bulk recombination (16, 28, 29). The observed behavior at the twin boundary suggests that any of these mechanisms is modified in a region extending a few micrometers away from the twin edge. Taking into account that the morphology observation assigns a capital role to chemical non homogeneity, either impurity or stoichiometry, in the formation of this twin, the segregation by the twin boundary of defects limiting the lifetime of carriers could be a reliable hypothesis in order to understand the behavior of the LO like band. In fig. 28 is clearly seen that the LO - plasmon coupled mode becomes more plasmon like as the twin boundary is approached, this should account for a larger intrinsic carrier concentration in such localized areas as compared to the regions placed far away from the twin edge, where higher laser power density is required to get a similar intrinsic carrier generation. In other words the intrinsic carrier concentration is higher than out of this region in the matrix. This could be the consequence of defect segregation that would result in an enhancement of the mean lifetime of the intrinsic carriers as a consequence of the decrease of the bulk recombination efficiency. Other effects, as band bending at such a region could also contribute to this effect; in fact a small enhancement of the second order Raman intensity is observed in this region, which could support this contribution.

Another important point is the observation of a TO phonon like peak in the regions neighboring the matrix-twin edge. This peak is forbidden in this scattering configuration and its observation reveals the break down of the Raman scattering selection rules. This can be related to residual stress or the existence of a partially misoriented transition region. Surprisingly this is only seen in the matrix side and extends only a few microns away from the edge line; this distance roughly corresponds to the enhanced carrier generation region previously reported; when the microprobe crosses the twin boundary

entering the twin volume an intense phonon-like TO peak, together with a a rather weak LO peak are observed. Apparently the existence of a misoriented region is the most reliable hypothesis to account for the observation of the forbidden TO peak in the twin-matrix boundary. It should be pointed out that in the cleaved plane small frequency shifts are recorded at the (110) matrix- (110) twin edge, which might be due to the existence of residual stress in this boundary region.

The analysis of the Raman spectrum in the cleaved (110) plane reveals interesting aspects related to the properties of the twin lamellae. In this plane the backscattering Raman selection rules allow only the TO mode, being the LO forbidden. The linewidth of the TO mode obtained across a scanning line crossing transversally the boundary region is represented in fig.29. Different considerations might be pointed out from this result. Firstly the linewidth is larger in the twin than in the matrix. At the twin-matrix boundary is recorded the narrowest peak. The width increases in the matrix up to a value similar to that measured in the twin at 5-6 μm away from the edge, then it decreases to the average value measured in the matrix around 10 μm far from the edge. It should be noted that the width of the TO peak in the regions of the wafer far from the twin, which are seen to be defect free, is narrower again (4.5 cm^{-1}).

The polarization Raman selection rules were also studied. It is seen that the region surrounding the edge is partially misoriented as deduced from the change in the depolarization ratio for $z<\text{yy}>z$ and $z<\text{xy}>z$ scattering configurations ($x=<001>$, $y=1/\sqrt{2} <110>$, $z=1/\sqrt{2} <110>$), fig.30. This is consistent with the observation of the forbidden TO peak in the (100) plane in the regions nearby the matrix-twin edge.

These results suggest that the twin-matrix boundary is a region of defect segregation, which could account for the low bulk recombination rate resulting in higher photogenerated carrier concentration in this area. This low defect concentration could also account for the narrow TO Raman peak in this region as compared to the other scanned zones; it is also rather probable that this edge corresponds to a stress relaxation region, which is consistent with the bending of the growth striations. From the edge to about 6 μm away in the matrix the TO peak is broadened reaching the average value measured in the matrix volume, it should be noted that this corresponds to the zone where the highest photogenerated electron concentration was estimated; beyond this distance the width

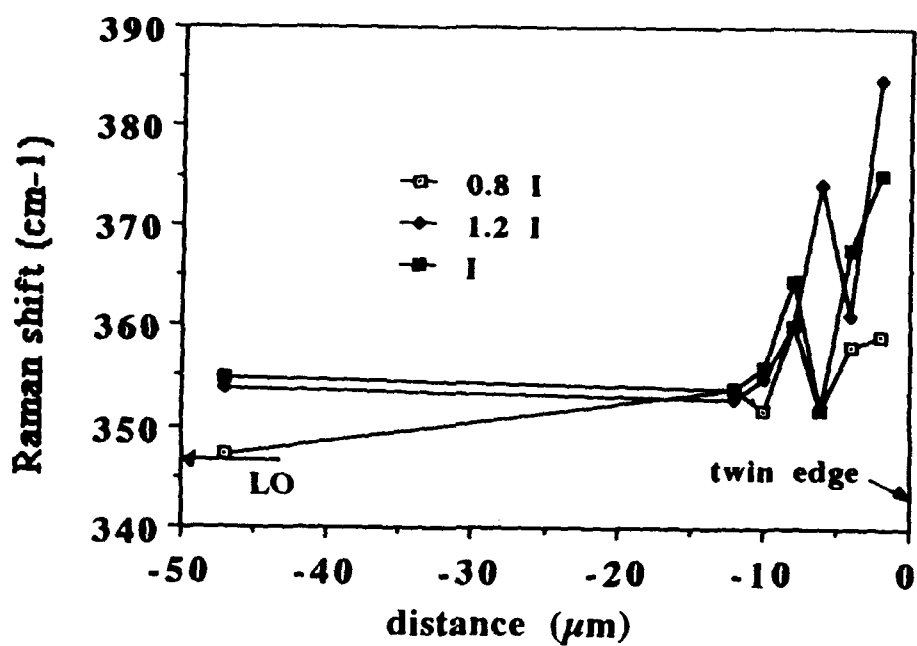


Figure 28: Raman shift of the LO like mode for increasing laser power density obtained at different points across a scanning line transversal to the matrix-twin boundary.

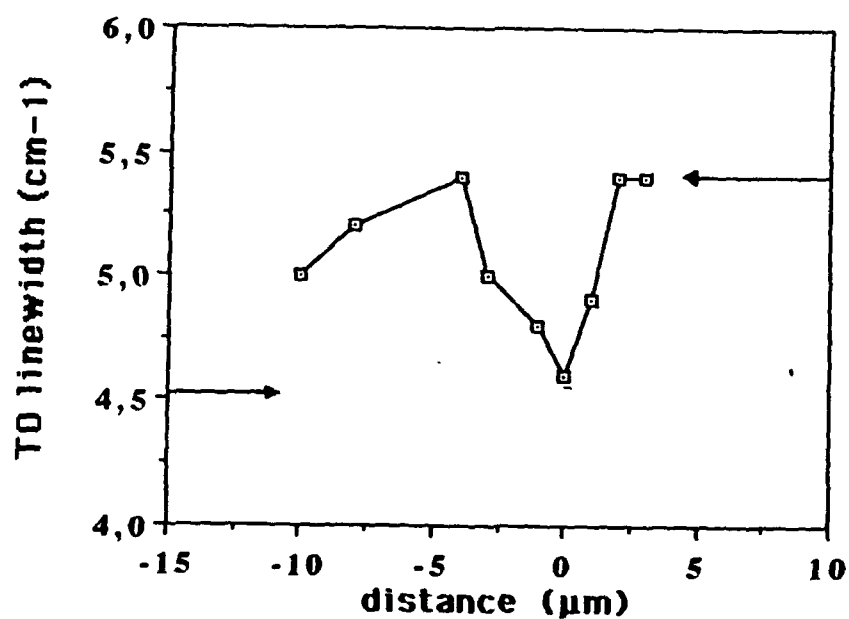


Figure 29: Linewidth of the TO phonon across a scanning line crossing the twin lamellae in the (110) cleaved line. The horizontal lines correspond to the linewidths inside the twin region (right) and out in the region far from the twin (left).

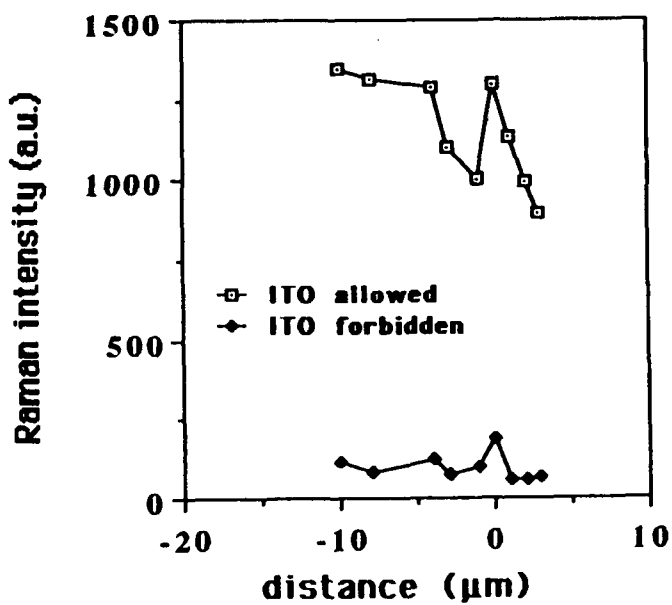


Figure 30: Intensity of the TO peak for $Z<\text{YY}>Z$ (allowed) and $Z<\text{XY}>Z$ (forbidden) scattering configurations ($X=\langle 001 \rangle$, $Y=1/\sqrt{2}\langle 110 \rangle$, $Z=1/\sqrt{2}\langle 110 \rangle$).

decreases to the average value detected in the regions of the matrix near the twin. It should be noted that far from the twin in the region where the cleaved plane was flat and no growth striations were seen the width of the TO peak is 4.5 cm^{-1} , which is close to the value measured in the twin-matrix edge, which is consistent with the assumption made about the segregation of defects at the edge. The fact that inside the twin the TO mode is broad can be associated with the high defect concentration of the twined volume as deduced from the highly irregular photoetching pattern characterizing these surfaces. All that seems to suggest that strong deviations from stoichiometry, resulting in variable growth rates, would be at the origin of the formation of this twin lamellae in undoped LEC InP.

Grown-in dislocations

Some grown-in dislocations were scanned in Sn-doped material, showing local misorientation and carrier depletion in the atmosphere of the dislocation. The line scans crossed the micron size atmospheres of the dislocations. Raman parameters along the scanning line are represented in fig.31. The main observations are:

- Partial misorientation as deduced from the TO / LO Raman intensity ratio in the atmosphere of the dislocation.
- Carrier depletion as deduced from the phonon like character of the Raman peaks. This is consistent with impurity segregation.
- Low carrier photogeneration rate, which can be accounted for by an enhanced carrier recombination in such area.

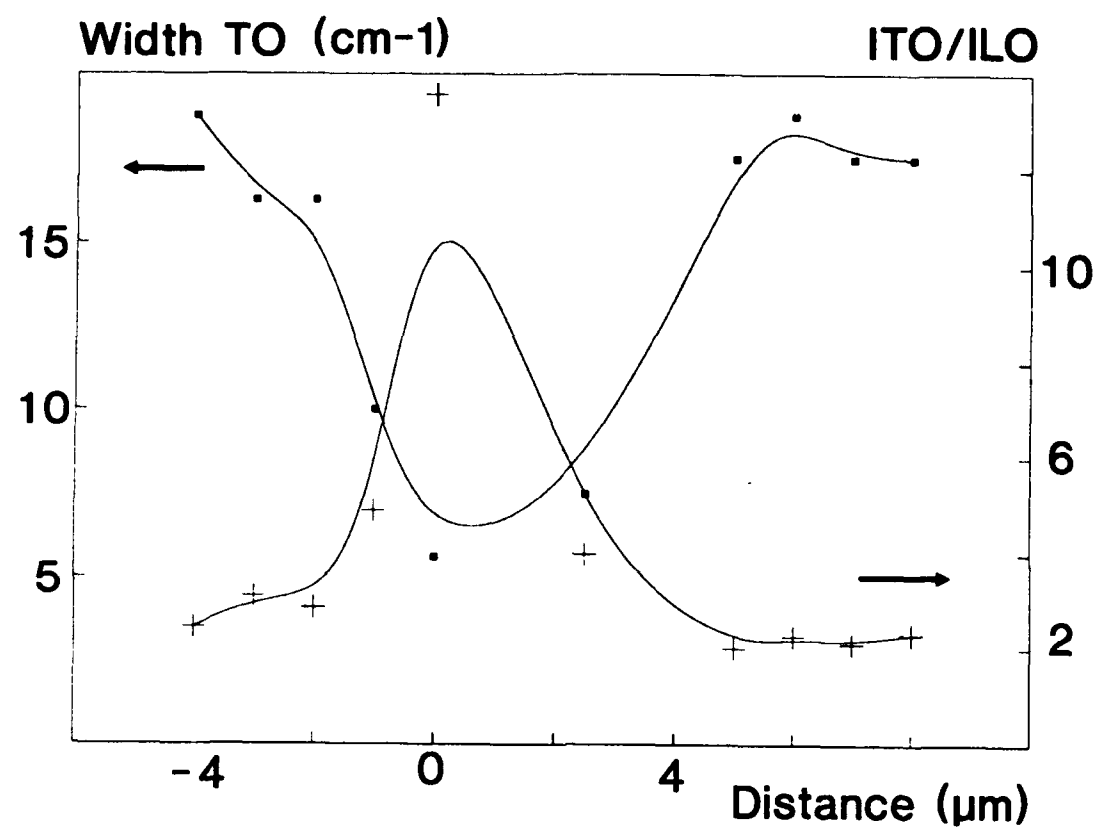


Figure 31: Raman parameters around a grown-in dislocation in Sn doped InP.

SPATIALLY RESOLVED PHOTOCURRENT

Semiinsulating InP

The state of the art of semiinsulating InP is based today on iron doping. Iron is added to the melt and its distribution in the crystal is controlled by its segregation coefficient. Due to the small value of this coefficient (1.7×10^{-3}) (1) its concentration increases from seed to tail and decreases from the growth axis to the edges of the ingot.

Different kind of impurity non homogeneities are usually found in these materials.

-Precipitates, the formation of impurity precipitates during the post growth cooling is due to a dopant concentration above the solubility limit (31,32).

-Growth striations. These impurity concentration variations are found along and transversally to the growth axis. They are due to different fluctuations typical of LEC growth process, such as non axial symmetry of the temperature field, varying interface kinetics, vibrations, non flat solid liquid interface due to unsteady convection (33,34)

-Dislocation atmospheres. An efficient gettering of impurities takes place at the dislocations.

These non-homogeneities of the impurity concentration result in changes in the local electric parameters, i.e. resistivity, mobility, minority carrier lifetime; which are a trouble for large integration densities.

Iron impurity

Iron is a substitutional impurity that occupies the cation site in the InP lattice. It introduces a deep acceptor level that compensates the residual shallow donors, mainly S and Si. Depending on the compensation ratio it can be either neutral Fe^{3+} or singly ionized Fe^{2+} (35).

The $Fe(3+/2+)$ level is splitted by the crystal field in two acceptor levels, the ground state, $5E$, and the excited state, $5T_2$ according to the scheme given in fig.32. The study of these levels has been carried out by different experimental techniques (35,36,37). Among these techniques, photoconductivity (36,37) provides useful information on the main

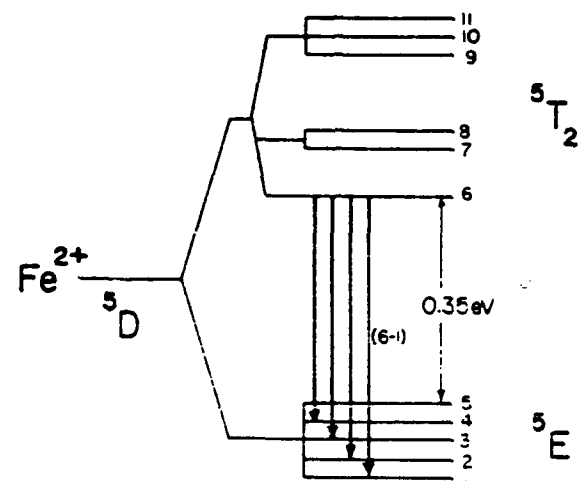


Figure 32: The crystal field : spin orbit splitting of the ^5D ground state of Fe^{2+} (3d^6) in a tetrahedral environment

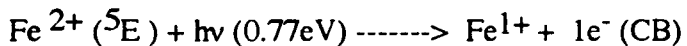
electronic transitions involving iron levels.

Photocurrent measurements

Photocurrent measurements were carried out either in a conventional way or under microscope excitation. Conventional measurements were carried out to study the main photocurrent transitions observed in this material in order to understand the origin of the contrast in the scanning photocurrent measurements.

The photocurrent spectrum was obtained under continuous light excitation. The samples were cut in parallelepipeds of $6 \times 3 \times 0.5 \text{ mm}^3$. They were provided of alloyed Indium contacts and mounted in the cold finger of a closed circuit helium gas cryostat. The optical excitation was made with light of an halogen lamp passing through a monochromator and an interference filter set in order to avoid high order light components.

A typical photocurrent spectrum is shown in fig. 33, it consists of two main photocurrent bands at 0.77 eV and at 1.2 eV, with a threshold at 1.08 eV. The low energy band is usually ascribed to an electronic transition involving the excitation of an electron from the ground state of Fe^{2+} :



The high energy photocurrent band is associated with the optical ionization of neutral Fe^{3+} :



The transitions involved are summarized in the level sketch of fig.34 .

The optical cross sections for electrons and holes are shown in fig.35, according to ref 38; showing that the low energy side of the spectrum ($<0.8 \text{ eV}$) is dominated by the excitation of electrons, while the high energy side ($0.8 \text{ eV} < h\nu < 1.29 \text{ eV}$) corresponds mostly to the excitation of holes. At 1.29 eV both cross sections equalize. This "magic"

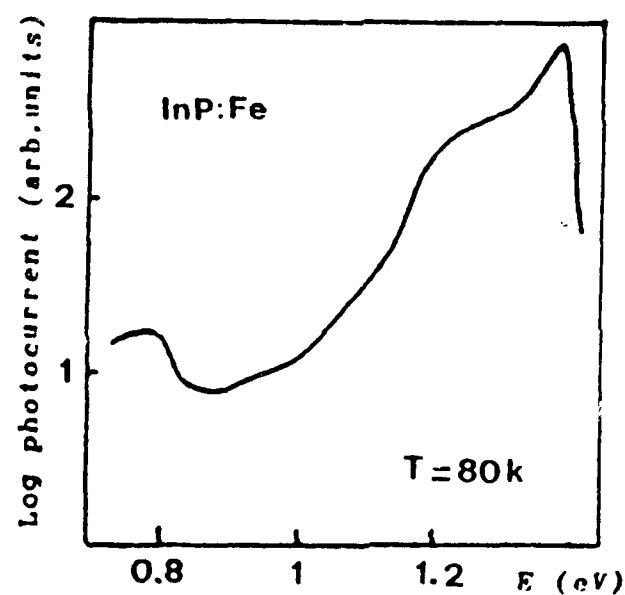


Figure 33: Typical photocurrent spectrum in InP:Fe obtained in a conventional way.

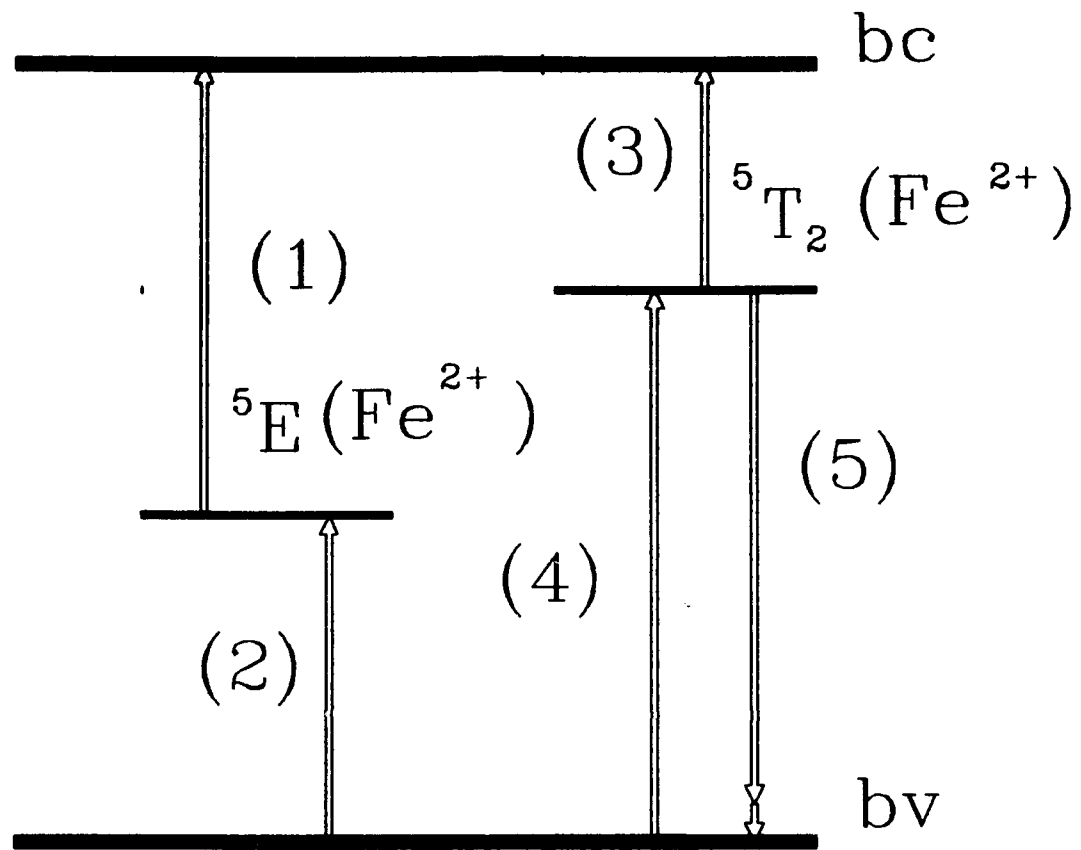


Figure 34: Flat band level sketch diagram, showing the main electronic transitions concerning Iron levels.

- 1) $\text{Fe}^{++}(\text{5E}) + 0.77 \text{ eV} \longrightarrow \text{Fe}^{+++} + 1\text{e}^- (\text{CB})$
- 2) $\text{Fe}^{++}(\text{5E}) + h\nu > 0.77 \text{ eV} \longrightarrow \text{Fe}^+ + 1\text{h}^+ (\text{VB})$
- 3) $\text{Fe}^{++}(\text{5T}_2) + \text{KT} \longrightarrow \text{Fe}^{+++} + 1\text{e}^- (\text{CB})$
- 4) $\text{Fe}^{+++} + 1.1 \text{ eV} \longrightarrow \text{Fe}^{2+}(\text{5T}_2) + 1\text{h}^+$
- 5) $\text{Fe}^{++}(\text{5T}_2) \longrightarrow \text{Fe}^{+++} + h\nu (1.08 \text{ eV})$

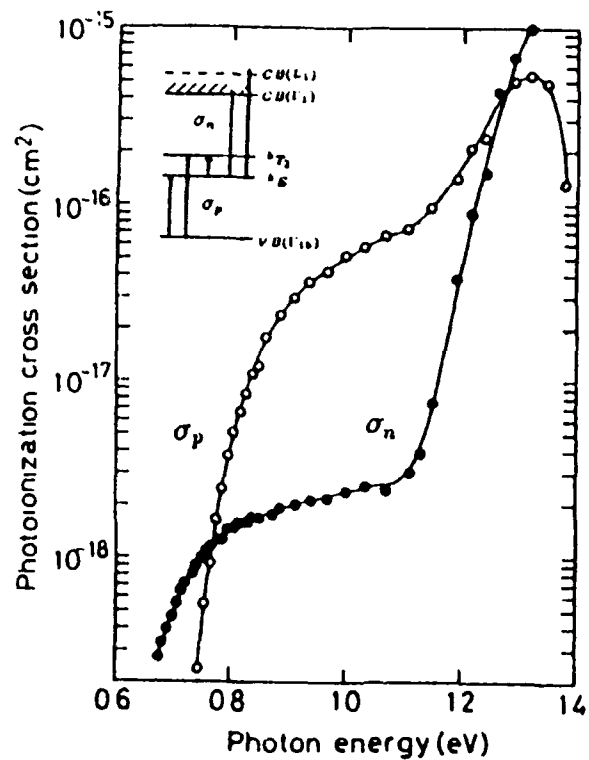


Figure 35: Iron optical cross section of electron and holes in InP:Fe.

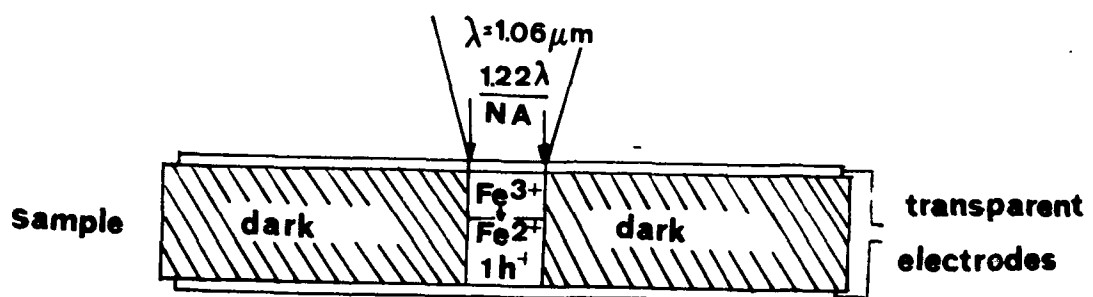


Figure 36: Sample configuration and principle of the method

wavelength can be used for the evaluation of the total substitutional iron concentration in optical absorption measurements.

Spatially resolved photocurrent

Photocurrent is a quite sensitive technique that allows to get information on bulk deep levels. It allows to work with commercial wafers, contrarily to optical absorption measurements that need thicker samples in order to have enough contrast for mapping iron distribution.

We have developed an experimental set up to study Spatially Resolved Photocurrent (SRP) in semiinsulating wafers. The basic elements of the experimental set up were shown in section 2, fig. 3.

The illumination source can be either a laser or an halogen lamp filtered through a monochromator or an interference filter set. The size of the spot depends on both the illumination source and the microscope objective used. Under laser excitation the diameter of the spot on the focal plane is diffraction limited, while under monochromatic light the region illuminated is determined by the microscope light field; which covers an area larger than 10^4 cm^2 .

The microscope is equipped with several objectives with Normarski optics in order to have a high contrast morphologic view of the samples surface. The samples are mounted on a cryostat specially designed for the microscope X-Y stage. The motorized X-Y stage has an accuracy of $0.25 \mu\text{m}$.

The system is controlled by a computer, that allows also to store the data measured by means of an interfaceable digital electrometer (Keithley 616)

The sample is provided of two transparent electrodes, on both the upper and the lower sides of the wafer, forming a sandwich contact configuration. Different metals were sputtered, showing that gold gave the best transparency together with the best metallic performance.

The principle of the method of measurement is basically described as follows, fig.36:

The volume in darkness is high resistive ($>10^9 \Omega\text{-cm}$ at liquid nitrogen temperature), focalizing the light beam through the microscope optics the illuminated volume increases its conductivity several orders of magnitude, thus the electric current measured corresponds to the photocurrent of this volume. By moving the X-Y stage, photocurrent scans can be performed, the speed of the scan can influence the photocurrent profile, depending on the local photocurrent transient. This can provide information on the distribution of different photogeneration and trapping mechanisms.

Three different laser wavelengths were used; $1.06 \mu\text{m}$ and $1.32 \mu\text{m}$ from a YAG laser and $0.62 \mu\text{m}$ from an He-Ne laser. The YAG laser excitations correspond to extrinsic carrier generation, while the He-Ne laser excitation correspond to e-h pair generation. In addition to this the penetration depth of the different probe lights is different from each other; while InP is transparent to YAG lines, the He-Ne line is strongly absorbed at the surface, probing so different electronic processes from each other. YAG is probing bulk properties, while He-Ne is probing surface properties.

We present in the next sections the results obtained for these wavelengths:

0.61 μm .-

Carrier generation with $0.61 \mu\text{m}$ light (He-Ne laser) consists of electron-hole pairs, which the lifetime is limited by surface and bulk recombination. In InP the surface recombination velocity is very low (26,27,28), so defect recombination centers play an important role concerning the lifetime of these carriers, which is limiting the photocurrent response. It is assumed that Fe^{2+} is an active recombination center and is responsible for the killing of the near band gap photoluminescence. A photocurrent scan is shown in fig.37, showing a decrease of the photocurrent from centre to edge of the wafer. This is consistent with the radial iron distribution. Some spike structures are observed. A three dimension map was performed showing the presence of these structures, fig.38, which are associated in some cases to subsurface damage, thus revealing the changes of the local compensation in these areas. It should be noted that out of these structures the presence of local short range fluctuations cannot be appreciated, contrarily to what happens for the

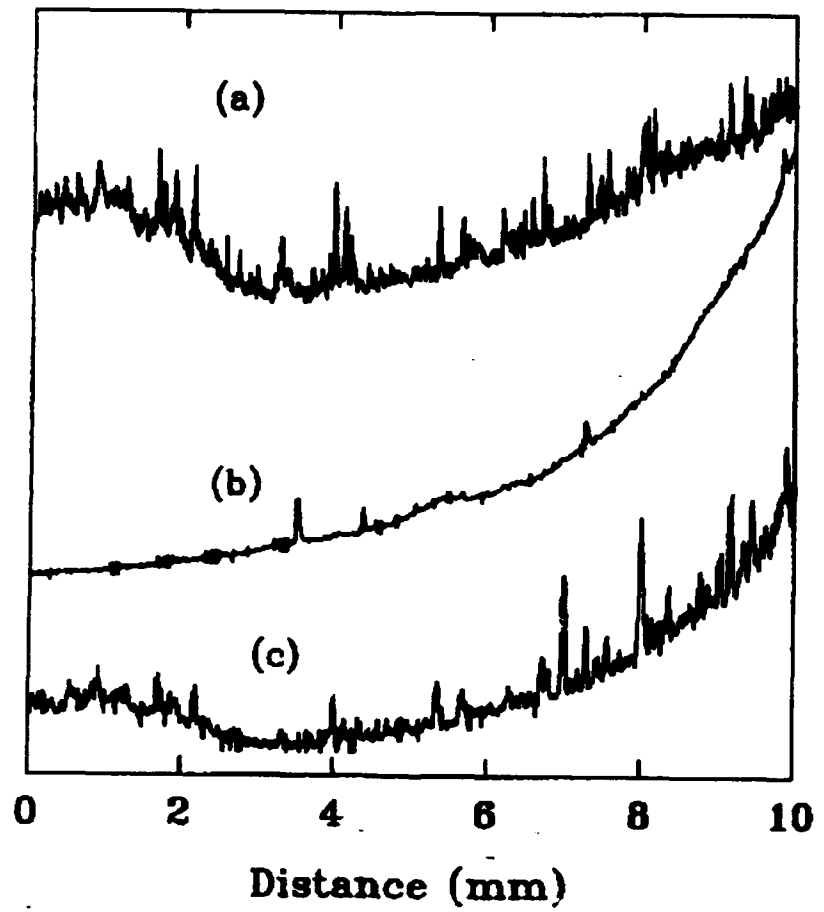


Figure 37: Photocurrent scans at different probe lights (a= 1.06 μm , b= 0.6 μm , c= 1.32 μm).

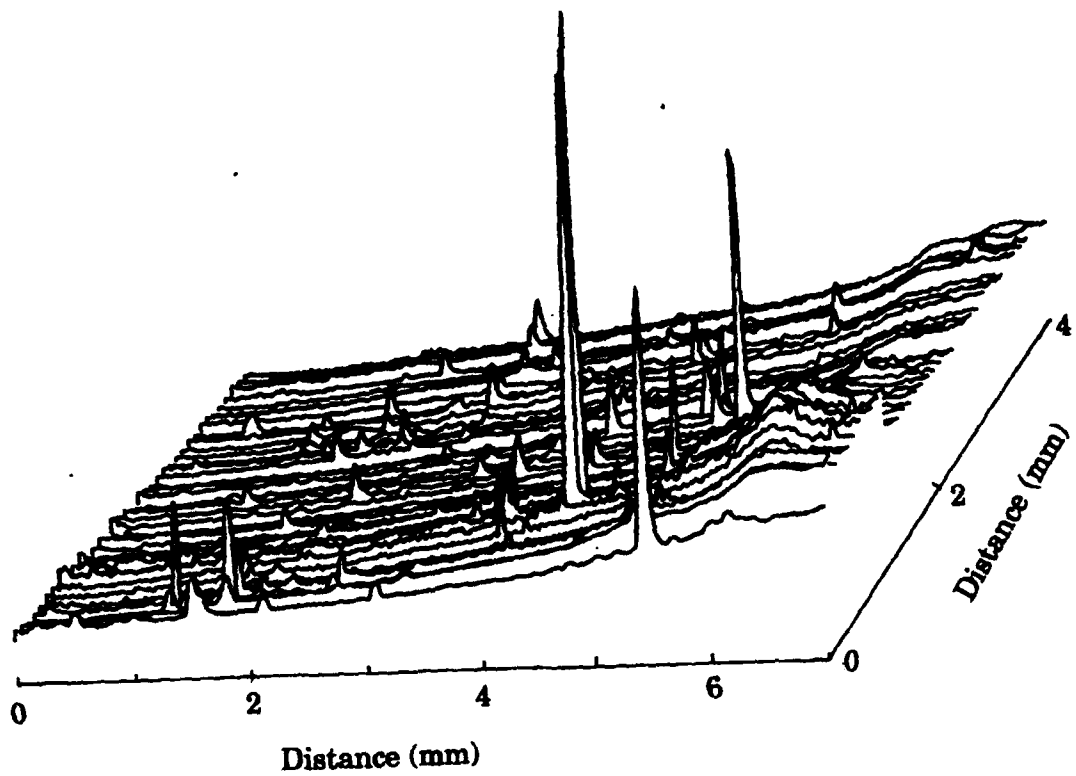
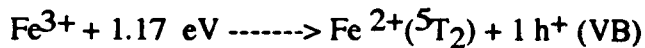


Figure 38: $0.61 \mu\text{m}$ photocurrent map.

other wavelength probes. This suggests that the main limitation is surface recombination and Fe^{2+} centers, the last assertion is consistent with the iron segregation in InP. The presence of short range growth striations was not revealed, contrarily to this the long range distribution is well revealed, as it can be deduced from the photocurrent decrease from center to edge.

1.06 μm

An inspection of the optical cross sections, fig.35, reveals that the optical cross section for holes is nearly one order of magnitude (≈ 8.1) larger than the electron cross section; therefore the dominant electronic transition taking place for this wavelength excitation is the photoionization of neutral Fe^{3+} that is transformed in the excited state ($^5\text{T}_2$) of Fe^{2+} , according to the following transition:



This is summarized in fig.34, showing the main mechanisms of carrier photogeneration.

The photocurrent for such an optical excitation is a function of $[\text{Fe}^{3+}]$ concentration and the hole lifetime, which is limited by trapping and recombination. All the measurements were carried out at liquid nitrogen temperature, for which the resistivity of InP is very high above the noise level of our experimental system, therefore the photocurrent contrast is significantly enhanced as compared to higher temperatures for which the dark current is not negligible.

Photocurrent scans were carried out. In figs.39 and 40 are shown two of these scans across an $<110>$ diameter of Fe doped InP wafers. Conspicuous differences can be noted in relation to the excitation with $0.61 \mu\text{m}$ light excitation. These photocurrent scans are characterized by a background photocurrent level that roughly reproduces the long range inhomogeneity observed for $0.61 \mu\text{m}$ excitation, fig.37, and a series of spikes superposed to the background; constituting so two different types of photocurrent fluctuations, long range and short range. In fig.41 a photocurrent map over a large area of an Fe-doped sample is shown. The strong fluctuation in the central region contrasts with the flat photocurrent of the peripheral regions. The local fluctuations are enhanced in the regions where the photocurrent is higher and are smoothed in the regions of lower

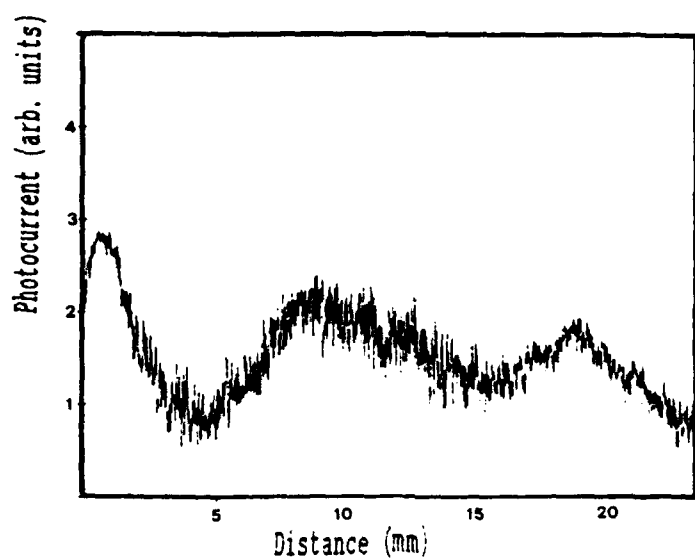


Figure 39: $1.06 \mu\text{m}$ photocurrent scan across an $<110>$ radii for an iron doped wafer (100). Sample a.

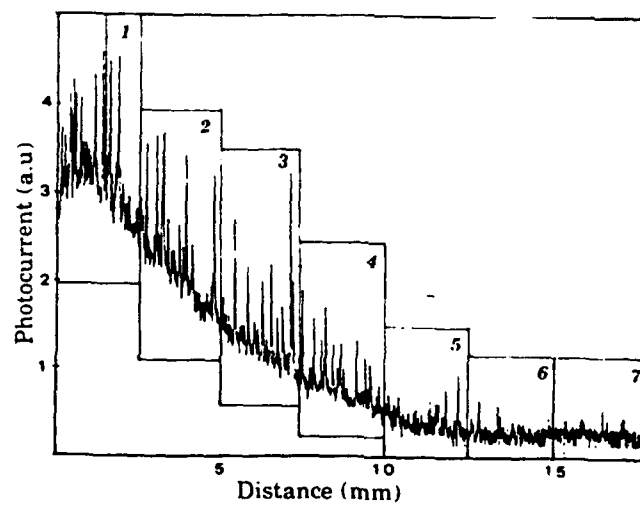


Figure 40: $1.06 \mu\text{m}$ photocurrent scan across an $<110>$ radii for an iron doped wafer (100). sample b.

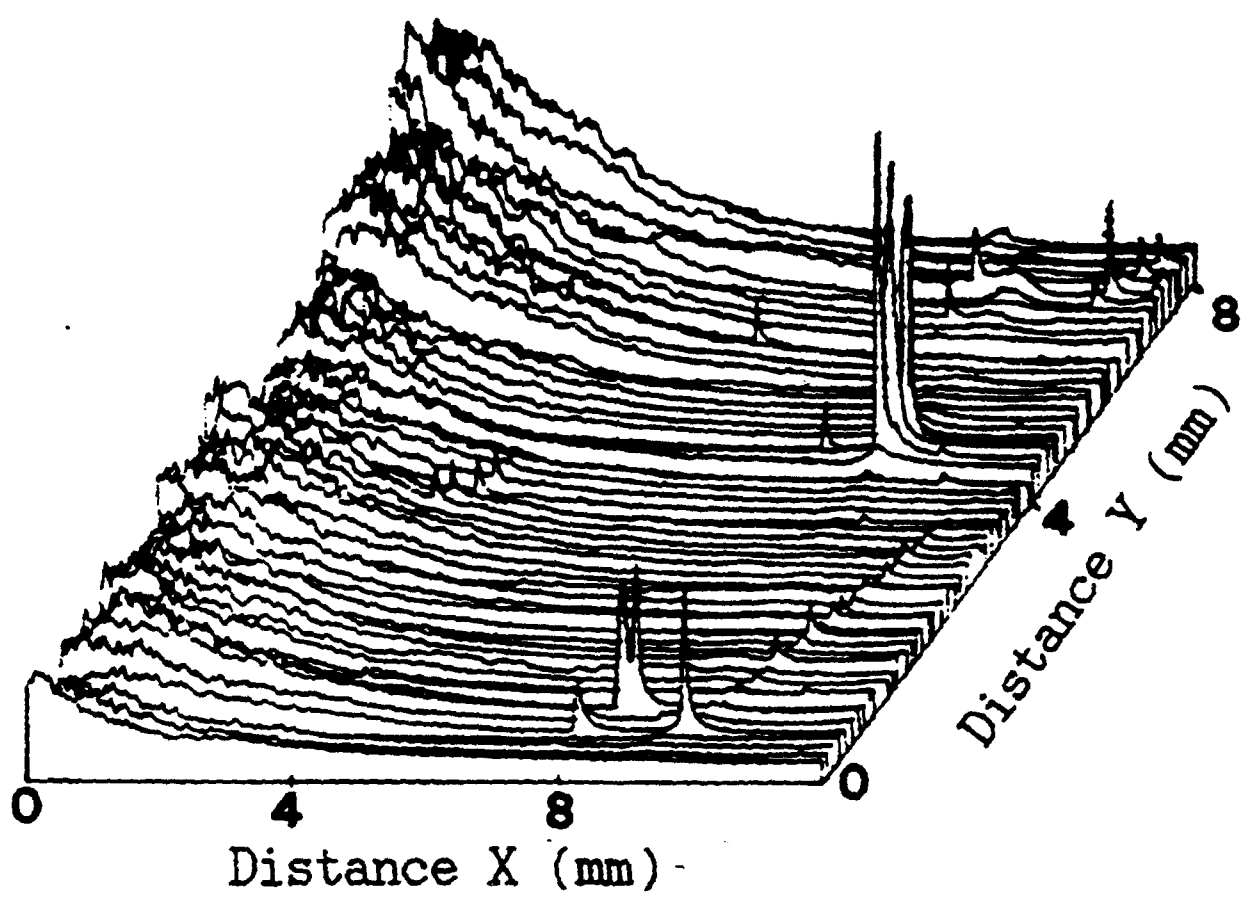


Figure 41: Photocurrent mapping of large region from an (100) wafer.

photocurrent, thus showing that the observed photocurrent changes do not correspond to noise in the acquisition system but they correspond directly to the local response of the sample to the laser beam.

Long Range Fluctuations

The long range photocurrent fluctuation profile across an $<110>$ diameter appears as:

*successive hills and valleys (Type A samples), fig.39.

*M shape (Type B samples), fig.40.

The periodicity of the successive hills and valleys is of a few mm (≈ 5 mm). The relative photocurrent intensity variations can get around 30-40 % of the average value. As it was stated before the photocurrent fluctuations are related to fluctuations in the $[Fe^{3+}]$ concentration; in fact 1.17 eV eV photocurrent is mainly due to holes resulting from the photionization of neutral Fe^{3+} . Anyway a full understanding of the trapping mechanisms is necessary in order to get a meaningful assessment of the photocurrent contrast. we will discuss later this point.

A map of a large area of a sample of type B(pulled at Rome Air Laboratory) was shown in fig.41. It is clearly observed that the highest photocurrent is observed in the regions approaching the center of the wafer; as the edge is approached the background photocurrent level decreases and reaches a nearly constant value; this sample showed a relative good local homogeneity as compared to other samples, mainly in regions far from the center. This map gives a rough idea of the macroscopic distribution of neutral iron across the wafer. Other samples showed in the region near the edge the existence of faceting as appreciated by the observation of some photocurrent structures in such a region, fig.42.

Short Range Fluctuations

Superposed to the long range fluctuations, short range fluctuations are observed. The shape, periodicity and sharpness of these fluctuations are dependent on samples.

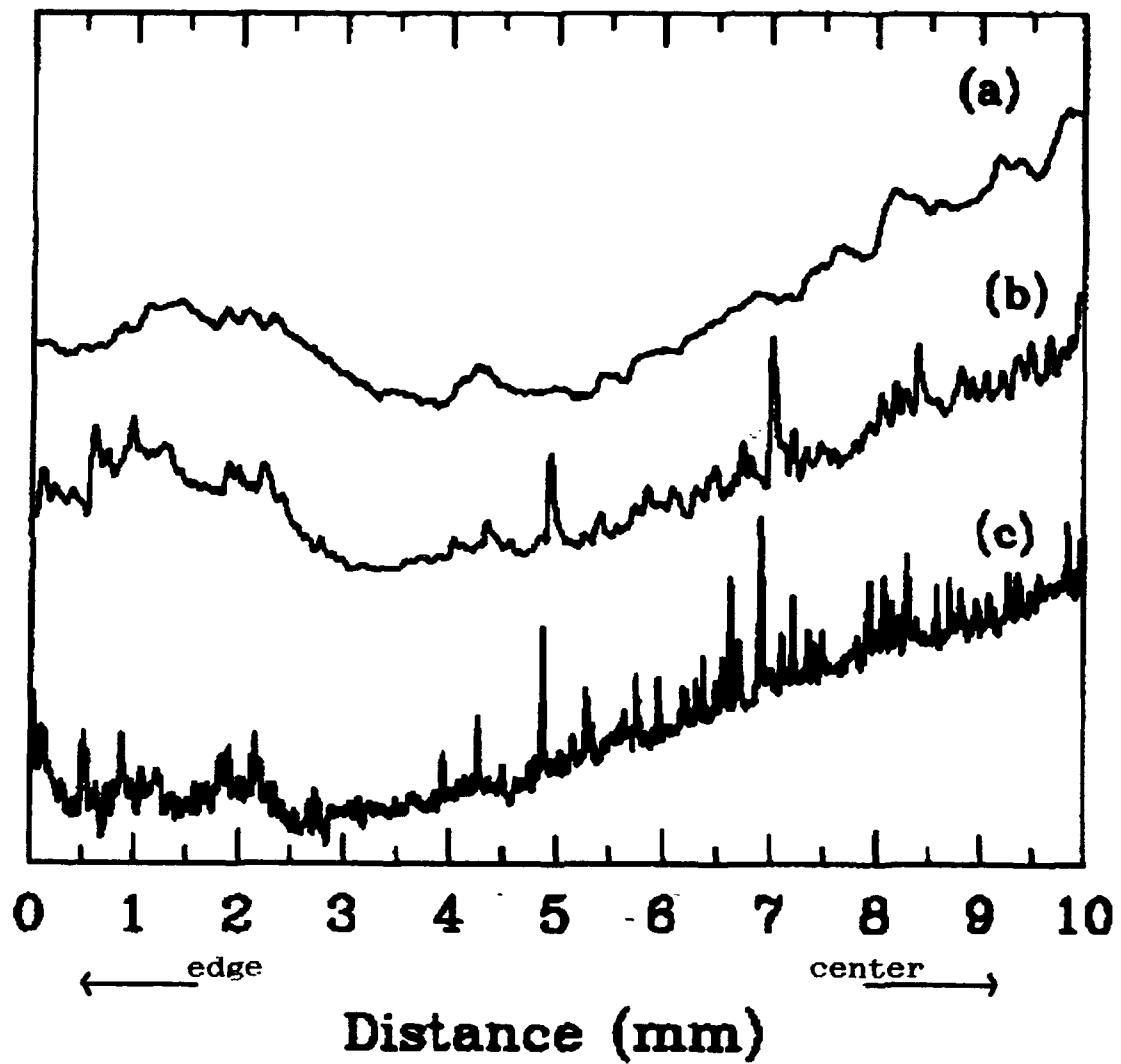


Figure 42: Photocurrent ($1.06 \mu\text{m}$) scans at different scanning speeds (a = $1250 \mu\text{m/s}$, b = $125 \mu\text{m/s}$, c = $5 \mu\text{m/s}$).

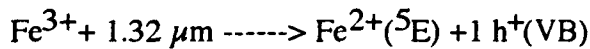
They appear either modulating the background photocurrent level or additively superposed to the background photocurrent level. The period of these fluctuations ranges from 70 to 150 μm , which fits well the dopant growth striation periodicity. The period of the fluctuations in samples of type A is shorter. In fig.43 the magnification of a photocurrent scan for different segments of the line scan are shown.

The most significant observation is the decrease of the photocurrent fluctuation as the wafer edge is approached. Though it would be more exact to say this that the higher the 1.06 μm photocurrent background level the larger the amplitude of the local fluctuation.

According to the nature of the 1.06 μm related photocurrent, these fluctuations can be ascribed in a first instance to variations of Fe^{3+} concentration in the substrate. This seems to imply that the $[\text{Fe}^{3+}]$ local fluctuation is enhanced in the regions where the $[\text{Fe}^{3+}]$ concentration is larger, while it is significantly flattened in the regions where the $[\text{Fe}^{3+}]$ is apparently smaller.

1.32 μm .

The optical cross section for holes is more than one order of magnitude (≈ 27.5) larger than the electron cross section for this wavelength; therefore the dominant electronic transition taking place for this excitation is the photoionization of neutral Fe^{3+} that is transformed in the ground state (^5E) of Fe^{2+} , according to the following transition:



The photocurrent scans obtained for this wavelength reveal the presence of structures similar to those obtained for 1.06 μm , i.e. long range variations and short range sharp structures, fig.37. This similarity accounts for similar carrier photogeneration mechanisms in both cases. In spite of this, there are regions where the correlation is not one to one; this point will be discussed later in relation to the trapping influence in the photocurrent contrast.

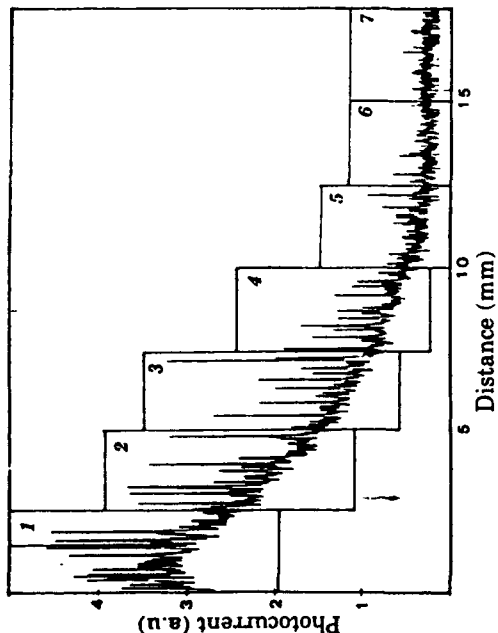


Figure 42: Photocurrent scan across $<110>$ radii for an iron doped sample. The plot shows Photocurrent (a.u.) on the y-axis (0 to 15) and Distance (mm) on the x-axis (0 to 2500). Seven windows are indicated by numbered rectangles: 1, 2, 3, 4, 5, 6, and 7. The signal shows a sharp peak at approximately 1250 mm.

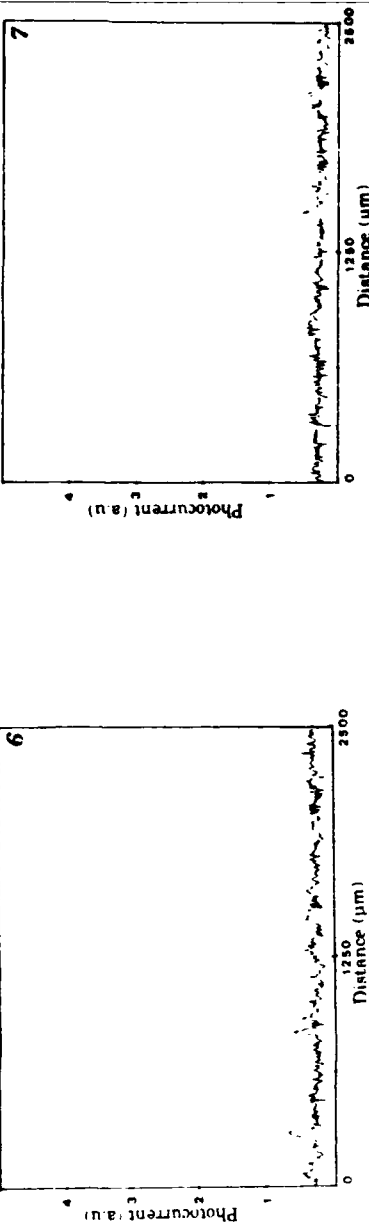
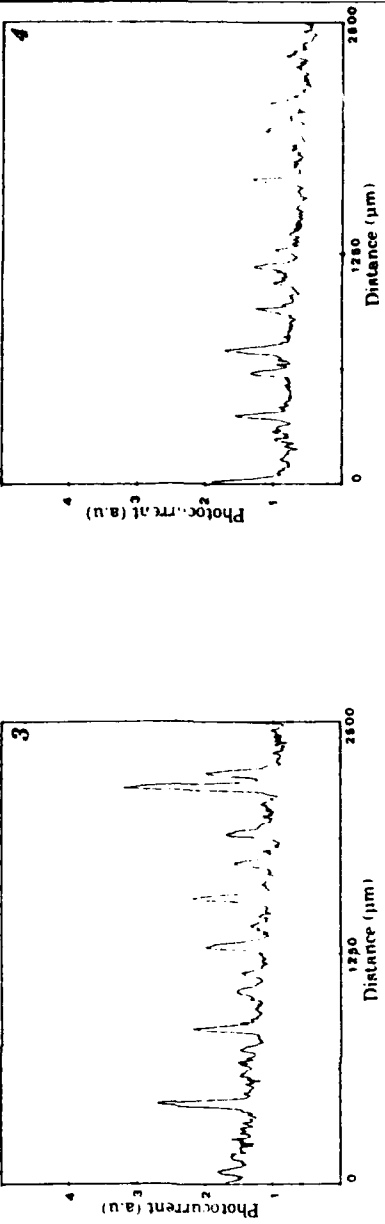
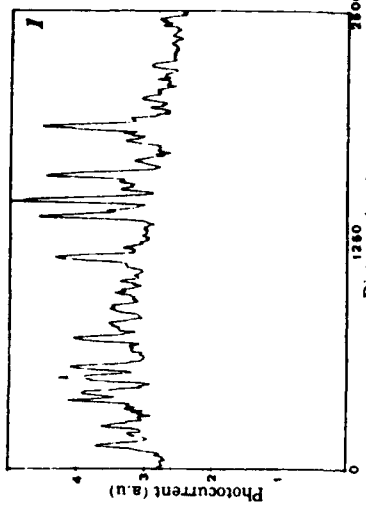
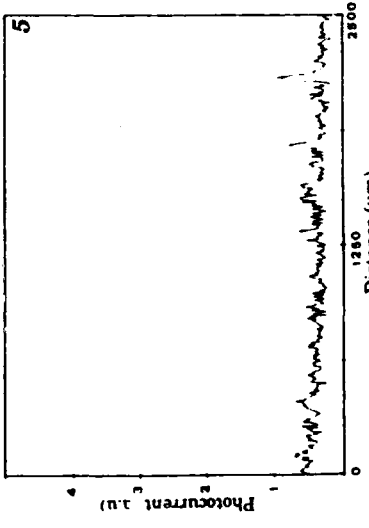
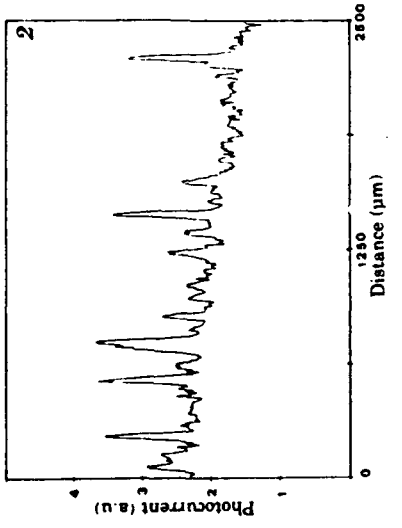


Figure 43: Photocurrent scan across $<110>$ radii for an iron doped sample and magnification of the windows indicated in the plot showing the local photocurrent fluctuations.



Discussion

A preliminary inspection of these photocurrent scans would suggest that these photocurrent structures are the result of the doping fluctuations associated with doping growth striations. Nevertheless large area photocurrent maps reveal that while for long range fluctuations this assumption is reasonable, it is not consistent for short range sharp structures that do not show the periodic two dimensional pattern characterizing this kind of fluctuations, fig.41. It should be noted that the photocurrent at a peak can get twice the value of the ground photocurrent level. This strong variation can hardly account for the low fluctuation related to short range doping growth striations (39,40). Therefore, we can say that these structures are rather associated with the presence of local non homogeneities, mainly at the dislocation areas. It should be noted that similar sharp structures have been reported to appear in PL maps of InP:Fe (40); nevertheless a one to one correlation between photocurrent and photoluminescence spike structures cannot be established at the present time, as far as we cannot establish a meaningful contrast understanding for both measurements.

The photocurrent sharp structures (spike) can be related to either strong carrier photogeneration associated with Fe^{3+} rich regions (heavily compensated) or Fe^{2+} depleted regions, which should give a low recombination rate, hence a long carrier lifetime. This last possibility will be the consequence of the existence of a low local net donor concentration, $N_D - N_A$; it might be consistent with the observation of sharp structures in PL maps. It should be noted that the $[Fe^{3+}] / [Fe^{2+}]$ ratio does not only depend on the total iron concentration but also on the net donor concentration ($N_D - N_A$) that is controlling the compensation ratio. This should imply that the observed $[Fe^{3+}]$ doping fluctuation could be related to the net donor concentration rather than to the total iron concentration. Though the most reliable hypothesis is that both would be non uniformly distributed.

It is also important to note that the electronic transitions involved for each of the excitation wavelengths, either 1.06 or 1.32 μm , can also significantly influence the profile of the photocurrent scan. In fact the photocurrent scans for 1.06 μm and 1.32 μm probe lights do not show a one to one correlation, showing that the photogeneration rates and the carrier captures are different from each other. Furthermore, this is

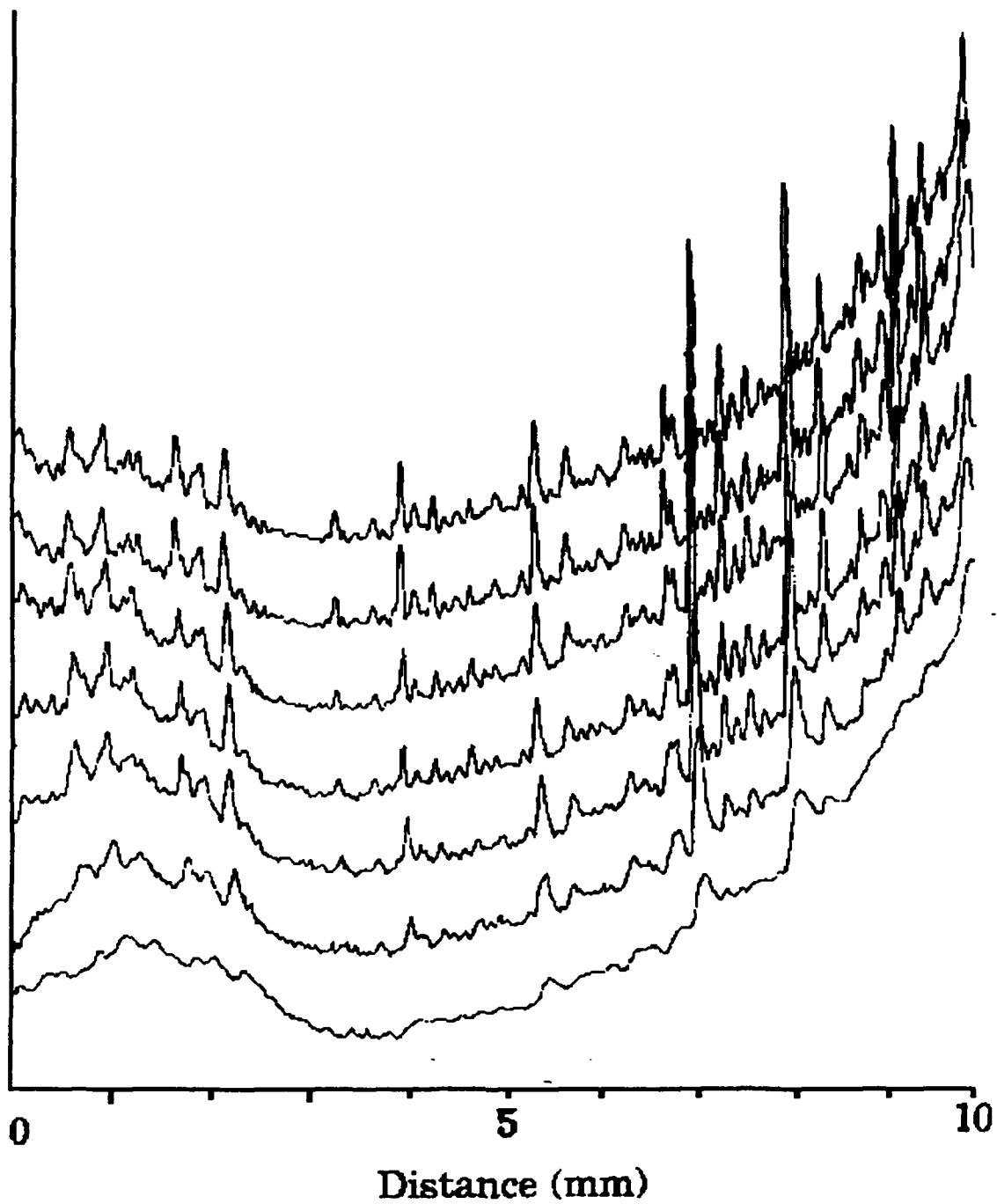


Figure 44: Photocurrent scans ($1.32 \mu\text{m}$) at different scanning speeds. Speed increase downwards.

confirmed by the dependence of both photocurrent scans with the scanning speed. While $1.32 \mu\text{m}$ scans are rather insensitive to the scanning speed; a decrease in the scanning speed results in a better resolution of the peaks without changes in the structures, fig.44. For $1.06 \mu\text{m}$ probe light the short range photocurrent structures undergo also some modifications depending on the scanning speed, fig.42. These changes can be understood in terms of the modification of the $[\text{Fe}^{3+}] / [\text{Fe}^{2+}]$ ratio under illumination as a consequence of trapping (41,42,43). It should be noted that the electron photogeneration is more efficient for $1.06 \mu\text{m}$ than it is for $1.32 \mu\text{m}$. In fact local fluctuations of trap concentration are expected to significantly affect the profile of the photocurrent scans (44). It should be pointed out that the changes in the photocurrent scans with the scanning speed are only a reflect of the the photocurrent transient at the different points probed. The relative variation between peaks and dips is much larger for $1.06 \mu\text{m}$ than for $1.32 \mu\text{m}$ probe light. As a general rule both probe lights give a larger photocurrent at the central area of the wafer and decreases as the edge is approached, see the large area map, fig.41. Some samples show also an increase of the photocurrent near the edge, which is consistent with the doping distribution of LEC growth. The $1.32 \mu\text{m}$ probe light lies in the spectral region of the photocurrent selfquenching (36,37), which implies a quick recombination at the ground state of Fe^{2+} , accounting so for a less effective trapping of carriers under this probe light; this is consistent with the small variation of the photocurrent lineshape with the scanning speed. Contrarily to what happens for the $1.06 \mu\text{m}$ probe light, for which trapping plays a dominant role in the photocurrent contrast (42,43,44). A photocurrent scan with $1.32 \mu\text{m}$ probe light superposed to the corresponding Nomarski micrograph is shown in fig.45. The photocurrent spikes appear related to the dislocation network. The average distance between photocurrent spikes is about $100-150 \mu\text{m}$ which fits well the average distance between dislocations.

High resolution topograms were performed by scanning the laser beam across reduced areas of the sample at a very slow scanning speed. This low scanning speed allows to get trapping equilibrium reducing so the non-homogeneities that could arise from the local changes in the trapping rate. These topograms are characterized by sharp structures, peaks or lines, superposed to a smooth photocurrent background level, fig.46. The area of these peaks ranges from a few to hundred square μm . The enhancement of the $1.06 \mu\text{m}$ and $1.32 \mu\text{m}$ related photocurrent levels resulting in such structures can be due



Figure 45: Nomarski micrograph and $1.32 \mu\text{m}$ photocurrent scan.

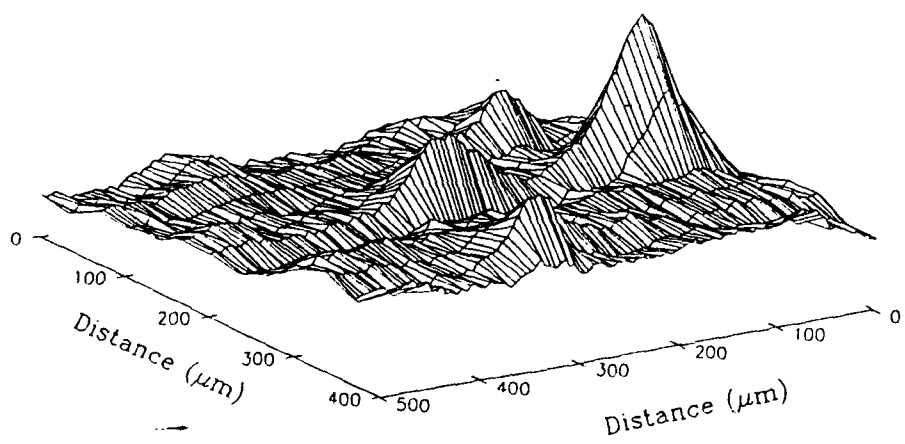
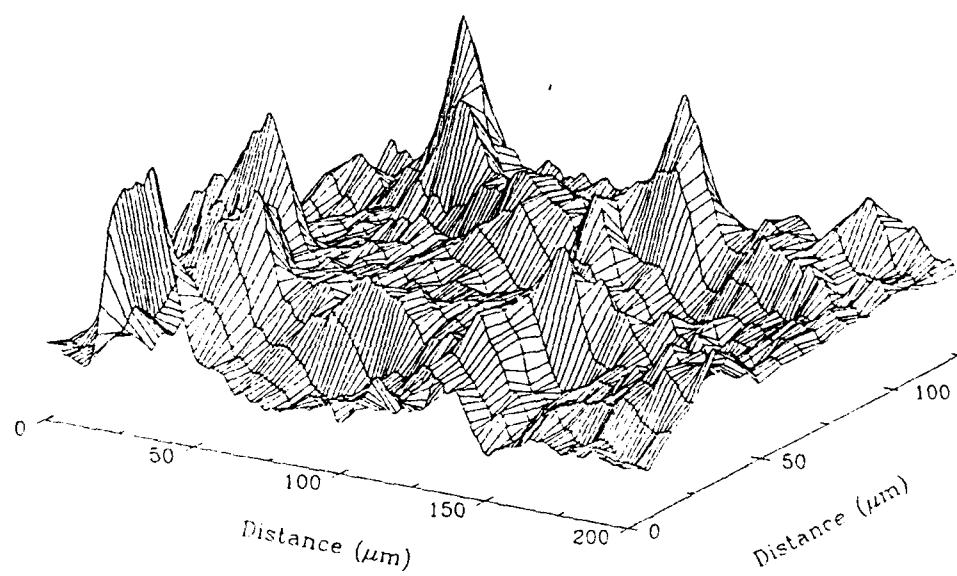
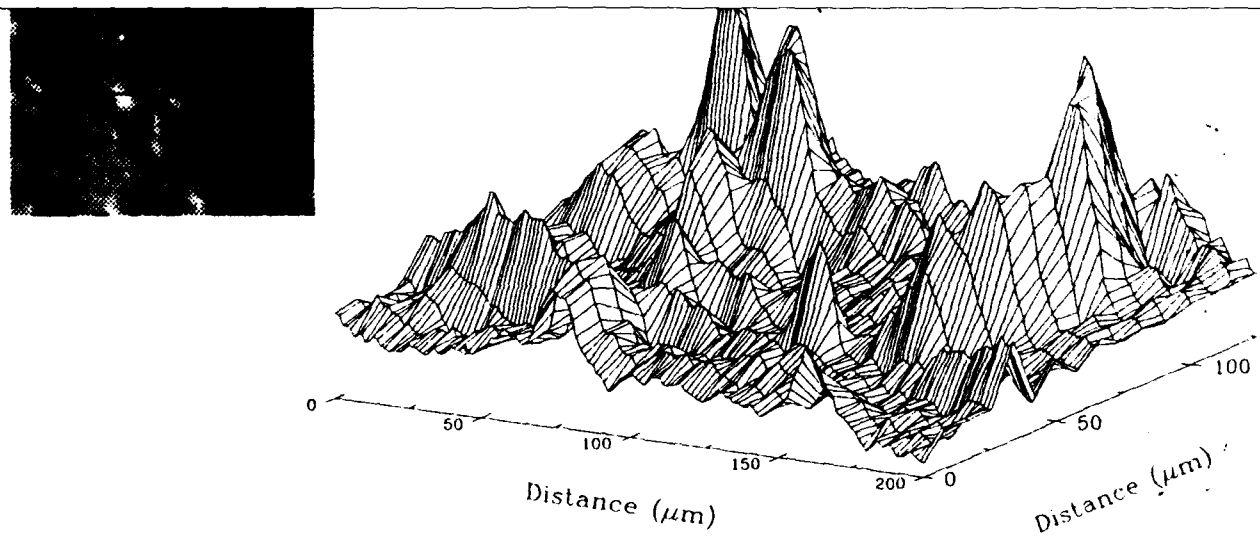


Figure 46: $1.06 \mu\text{m}$ photocurrent maps of small areas.

to either a local increase of the neutral iron concentration or an increase of the carrier lifetime. Similar structures were observed by other authors in photoluminescence measurements. It has been well stated that the photoluminescence contrast is enhanced in poor iron regions. Iron is an active non radiative recombination center in InP. Therefore it is usually assumed that the photoluminescence peaks are associated with iron depleted regions, while the dark photoluminescence areas correspond to gettered iron regions, such as dislocations. The relation between both photoluminescence and photocurrent topograms needs to be established in order to understand both the local electric compensation, through the $[Fe^{3+}] / [Fe^{2+}]$ ratio and the nature of the defects limiting the minority carrier lifetime.

Finally, an interesting observation is that no local photocurrent depressions have been seen which seems to suggests that the changes in the local defect concentration giving the photocurrent contrast are superposed to a uniform background. In this aspect the photocurrent maps are different to the PL maps, showing so the possible complementarity between both kind of measurements.

CONCLUSION

DSL is a powerful technique for revealing crystallographic defects in InP. It provides a morphologic description of the grown in dislocations, twins, growth striations, subsurface damage. The observation of these morphologic features by means of Nomarski microscopy and PSM (Phase Stepping Microscopy) provides a complete picture of the extended defects in InP. DSL photoetching is not so efficient as it is in GaAs, and long etching times are necessary in order to have a well contrasted defect revelation.

Raman spectroscopy has been used to study crystal perfection. As polished samples were characterized in terms of surface oxidation under ambient exposure, which result in band bending produced at the solid phosphorus - InP interface. This oxidation was found to be the cause of non homogeneity due to the non uniform oxidation.

Raman spectra obtained in InP under microprobe point illumination must be carefully analyzed, due to the strong carrier photogeneration that produces strong phonon- plasmon

coupling with the corresponding phonon screening. This carrier photogeneration is the result of the small surface recombination velocity in N-type and semiinsulating InP. Meanwhile p type material was shown to have a much higher surface recombination velocity, avoiding the observation of coupled phonon plasmon modes, bellow 10^{16} cm^{-3} hole concentration. In this context dopant non homogeneities were probed to partially control the intrinsic carrier concentration via extrinsic recombination. This was used in order to analyze some of the extended defects present in our materials.

Among these crystallographic defects microtwins, grown-in dislocations and growth striations were scanned by the Raman microprobe. The structural characteristics were unambiguously determined, showing the local crystallographic orientation of the twins and the grown-in dislocations through the Raman scattering selection rules. Additional information concerning the presence of electrically active atmospheres was acquired.

Spatially Resolved Photocurrent measurements provided a picture of the homogeneities related to iron impurity distribution in semiinsulating InP. This technique was revealed as very sensitive to determine the presence of electrical inhomogeneities related to the presence of iron. Different probe lights were used, each one revealed different structures at both short and long range scale. The structures revealed by $0.62 \mu\text{m}$ light were associated with surface defects, and differed from those obtained with the other probe lights. This photocurrent response is limited by both the surface recombination and the presence of Fe^{2+} , that is an active recombination center.

The other probe lights revealed conspicuous non-uniformities, showing strong relative variations. These non homogeneities are related to the local fluctuation of the neutral iron concentration $[\text{Fe}^{3+}]$. This appears clearly for $1.32 \mu\text{m}$ probe light, that showed a complete independence on how the excitation was done, apparently the obtained profile depends only on the $\text{Fe}^{3+} \rightarrow \text{Fe}^{2+}$ ionization process. Contrarily to this the profiles obtained with $1.06 \mu\text{m}$ light showed a strong dependence with the experimental parameters, such as the scanning speed or the light intensity, revealing thus the importance that trapping has on the photocurrent contrast for this wavelength.

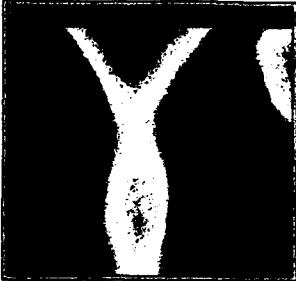
High resolution maps were obtained revealing strong non homogeneities in the wafers studied. The fact that growth striations are revealed evidences that there other sources of

non- uniformity, presumably localized in the dislocation atmospheres, that present much stronger iron related distribution fluctuations than growth striations. These fluctuations are enhanced in the regions with enhanced photocurrent background, showing thus in an indirect way that the higher the iron concentration the higher the local fluctuation.

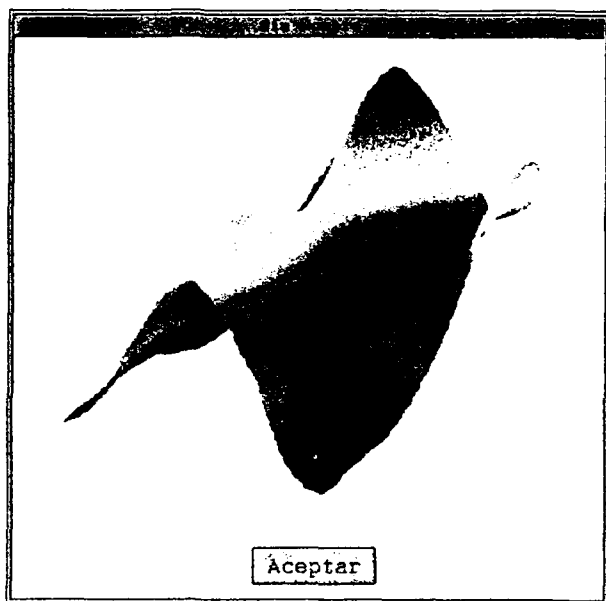
REFERENCES

1. G.Müller; *Phys.Scripta* **t35**, 201 (1991)
2. K.Ssumino; Defect and properties of semiconductors: Defect Engeneering (Ed J.Chikawa K.Sumino and K. Wada, KTK Scientific Publishers Tokio 1987) p3.
3. R.Beserman, C.Cyberman, R.Brener, J.Laborde, I. Salzman, M.Weyers, A.Braners, P.Balk; *Appl.Phys.Lett* **56** 919 (1990).
4. G.P.Schwartz, U.K. Chakrabarti, R.A. Landise, A.J.Caporaso; *Appl.Phys.* **65**, 2154 (1989).
5. B.Boudart; Ph. D (Strasbourg-France). 1992.Unpublished.
6. O.Mizumo, H.Watanabe; *Electron.Lett.* **11**, 118 (1972).
7. S.Nakashima, M.Hangyo; *IEEE Journal of Quantum Electronics.* **25**, 965 (1987).
8. D.E.Apsnes, A.A.Studna; *Phys.Rev:B* **27**, 985 (1983).
9. J.Jiménez, M.A.Gonzalez, L.F.Sanz, L.R. de Angulo, J. Bonnafé; *Semicond. Sci. Technol.* **7**,202, (1992).
10. J.L.Weyher, J. Van De Ven; *J.Cryst.Growth* **78** 191 (1986).
11. J.L.Weyher; *Mater.Sci.Eng.* part B (to be published).
12. B.Prevot, J.Wagner; *Prog.Cryst.Growth and Charact.Mater.* **22** 245 (1991).
13. F.H.Pollak: Analytical Raman Spectroscopy, Ed by J.G.Groselli, B.J. Bulkin (J.Wiley, N.York 1991) Ch 6.
14. B.H.Bairamov, J.P.Ipatova, V.A.Milorava, V.V.Toporov, N.Naukkarinen, T.Tuomi,G.Irmen, J.Monecke; *Phys.Rev:B* **38** 5722 (1988).
15. B.Boudart, B.Prevot, C.Schwab; *Appl.Surf.Sci.* **50** 295 (1990).
16. G.Abstraiter, E.Bauser, A.Fischer, K.Ploog; *Appl.Phys.* **16** 345 (1978).
17. M.Herms, G.Irmer, J.Monecke, O.Oettel; *J.Appl.Phys.* **71** 432 (1092).
18. S.Nakashima, H.Yugami, A.Fujii, M.Hangyo, H.Yamanaka; *J.Appl.Phys.* **64** 3067 (1988).
19. K.Murase,S.Katayama, H.Kawamura, Y.Ando; *Prog.Theor.Phys.* **57**, 115 (1975).
20. A.Pinczuk, A.A.Ball, R.E. Nahory, M.A.Pollak, J.M. Morlock; *J.Vac.Sci.Technol.* **16**, 1168 (1979).
21. S.Onari, R.Trommer, M.Cardona; *Sol.Stat.Commun.* **19**, 1145 (1976).
22. M.Sinyukov, R.Trommer, M. Cardona; *Phys.Stat.Sol. B* **86**, 563 (1989).
23. D.J.Evans, S.Ushioda; *Phys Rev.B* **9**, 1638 (1974).
24. Z.Hang, H.Shen, F.H. Pollak; *J.Appl.Phys.* **64** 3233 (1988).

25. N.T.McDevitt, J.S.Solomon; *J.Electrochem.Soc.* **133**, 1913 (1986).
26. H.C. Casey, E.Buehler; *Appl.Phys.Lett.* **30**, 247 (1977).
27. T. Nakamura, T.Katoda; *J.Appl.Phys.* **55** 3064 (1984).
28. Y.Rosenwaks, Y. Shapira, D.Huppert; *Appl.Phys.Lett.* **57**, 2552 (1990).
29. J.Wagner; Th.Frey, W.Jantz; *Appl.Phys.Lett.* **51**, 1904 (1987).
30. J.Wagner; "Light Scattering in Semiconductors Structures and Superlattices" (Plenum, N.York 1991).
31. E.D. Bourret, A.G.Elliott, B.T.Lee, J.L. Jaklevic; 1987 DRIP II (Mater. Sci. Monographs. **44**) Ed. by E.R. Weber (Amsterdam, Elsevier) p.95.
32. R.P.León, M.Kaminska, K.M.Yu, E.R.Weber; *Phys. Rev. B* **46**, 12460 (1992)
33. M.Cocito, P.Franzosi, G.Sariati, F.Tiariol; *Scanning Electron Microscopy* **6**, 1299 (1986).
34. D.J.Carlson, D.Bliss; Proc.InP and Related Materials Conference (Newport Rode Island 1992 IEEE) p.515.
35. For a review see: S.G.Bishop in " Deep centers in semiconductors", ed. by S.T. Pantelides (Gordon and Breach, N.York 1985) **Ch 7**.
36. S.Fung, R.J.Nicholas, R.A. Stradling; *J.Phys. C* **12** 5145 (1979).
37. J.Jiménez, M.A.Gonzalez, V.Carbayo, J.Bonnafé; *Phys.Stat.Solidi a* **77**, k69 (1983).
38. T.Takanoashi, N.Nakajima; *J.Appl.Phys.* **65**, 3933 (1989).
39. W.Meier, H.Ch.Alt, Th Vetter, J.Volk, A. Winnacker; *Semicond.Sci.Technol.* **6**, 297 (1991).
40. S.Y.Longere, S.K.Krawczyk, R.Coquille, H.L'Haridon, P.N.Favennec; *J. Appl. Phys.* **68**, 755 (1990).
41. C.G.Kovalevskaya, V.I.Alynshina, S.U.Solobodchikov; *Sov.Phys.Semicond.* **8**, 1217 (1975).
42. R.Fornari, B.Santic, U.desnica; Proc:InP and Related Materials (IEEE, Newport 1992) p 511.
43. Z.Q.Fang, D.C.Look, J.H. Zhao; Proc:InP and Related Materials (IEEE, Newport 1992) p 634.
44. M.A.González, J.Jiménez, P.Martín, L.F.Sanz, M.Chafai, M.Avella . Space Charge Effects in Semiconductors, ed. by D.Nolte (MRS Proc. Pittsburgh 1992) p 241.



255



Aceptar